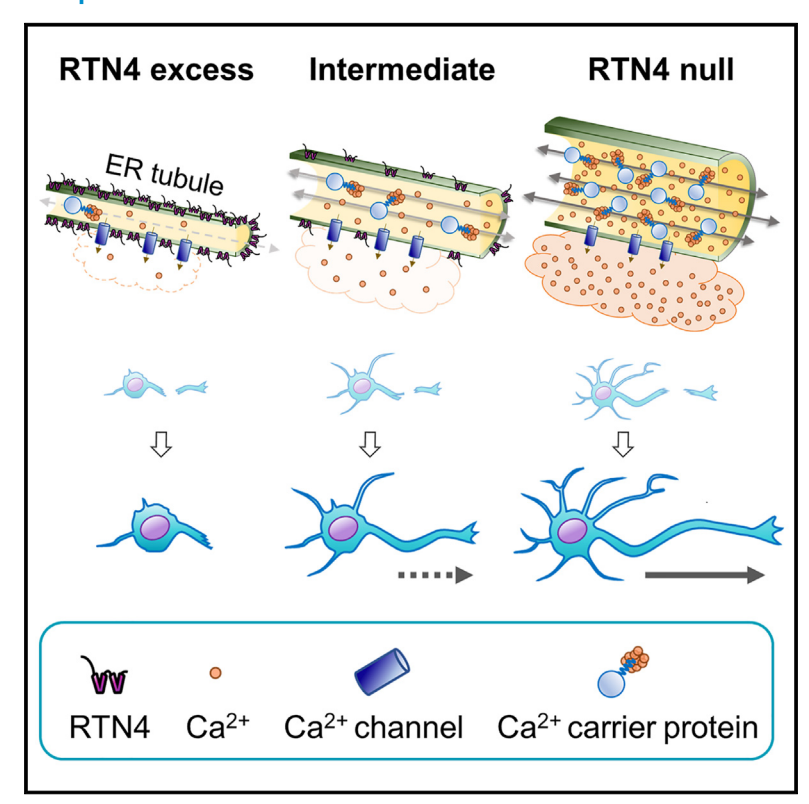
Endoplasmic reticulum morphology regulation by RTN4 modulates neuronal regeneration by curbing luminal transport

Graphical abstract



Authors

Tasuku Konno, Pierre Parutto, Cécile C. Crapart, ..., Laura M. Westrate, Elena F. Koslover, Edward Avezov

Correspondence

ekoslover@physics.ucsd.edu (E.F.K.), ea347@cam.ac.uk (E.A.)

In brief

Konno et al. report that reticulon 4 (RTN4), an endoplasmic reticulum (ER) morphogen also known as neurite outgrowth inhibitor (Nogo), negatively regulates the transport of ER luminal materials such as calcium by modulating the size of ER tubules, defining a direct link of ER morphoregulation to neuronal activity.

Highlights

- Neurite outgrowth inhibition effect of RTN4 originates from the ER
- Dose of RTN4 modulates the width of ER tubules
- RTN4 curbs local ER calcium release by hindering luminal transport







Article

Endoplasmic reticulum morphology regulation by RTN4 modulates neuronal regeneration by curbing luminal transport

Tasuku Konno,¹ Pierre Parutto,¹ Cécile C. Crapart,¹ Valentina Davì,¹ David M.D. Bailey,² Mosab Ali Awadelkareem,¹,³ Colin Hockings,¹ Aidan I. Brown,⁴,⁵ Katherine M. Xiang,⁶ Anamika Agrawal,⁴ Joseph E. Chambers,² Molly J. Vander Werp,⁵ Katherine M. Koning,⁵ Louis Mounir Elfari,⁶ Sam Steen,⁵ Emmanouil Metzakopian,¹ Laura M. Westrate,⁵ Elena F. Koslover,⁴,* and Edward Avezov¹,¹0,*

¹UK Dementia Research Institute at University of Cambridge, Department of Clinical Neurosciences, Cambridge CB2 0AH, UK

SUMMARY

Cell functions rely on intracellular transport systems distributing bioactive molecules with high spatiotem-poral accuracy. The endoplasmic reticulum (ER) tubular network constitutes a system for delivering luminal solutes, including Ca²⁺, across the cell periphery. How the ER structure enables this nanofluidic transport system is unclear. Here, we show that ER membrane-localized reticulon 4 (RTN4/Nogo) is sufficient to impose neurite outgrowth inhibition in human cortical neurons while acting as an ER morphoregulator. Improving ER transport visualization methodologies combined with optogenetic Ca²⁺ dynamics imaging and *in silico* modeling, we observed that ER luminal transport is modulated by ER tubule narrowing and dilation, proportional to the amount of RTN4. Excess RTN4 limited ER luminal transport and Ca²⁺ release, while RTN4 elimination reversed the effects. The described morphoregulatory effect of RTN4 defines the capacity of the ER for peripheral Ca²⁺ delivery for physiological releases and thus may constitute a mechanism for controlling the (re)generation of neurites.

INTRODUCTION

The endoplasmic reticulum (ER) is the single largest organelle, forming stacks of membranous sheets contiguously interconnected with a network of tubules that extends throughout the cell periphery. This architecture is thought to enable the ER to deliver its unique contents (e.g., Ca²+) throughout the cell and to supply numerous contact sites with other organelles (e.g., mitochondria, endo/lysosomes). However, the physical nature and structure-function relationship of the ER nanofluidic network remains obscure.

In terms of the generation of ER structure, considerable advances have helped elucidate how membranes can be curved to attain the ER's tubular morphology. In particular, a family of ER-shaping proteins has been identified and substantially characterized. Independently, a neuron-specific repertoire of these ER morphogens has emerged, and an increasing number of members are associated with neurodegenerative diseases

both biochemically^{2–5} and as hereditary causes.^{6–9} Remarkably, two ER-shaping proteins (among approximately two dozen known examples) were sufficient to reconstitute the ER structure *in vitro*.¹⁰ This suggests potential regulatory functions, other than simple morphogenesis, for at least some of the remaining non-essential morphogens, such as reticulon 4 (RTN4).

The RTN4 gene is a relatively late evolutionary acquisition (appearing with the advent of amphibians), dispensable for cell survival and morphogenesis of ER tubules. 11-13 Earlier studies designated RTN4 as Nogo, reflecting its axonal plasticity-restricting properties. 14 An excess of Nogo/RTN4 splice variants limits axonal regeneration, 15-17 while its knockout (KO) improves the process in animal models. 11,12 A prior work suggested a model where outgrowth inhibition (the Nogo effect) results from RTN4 on an oligodendrocyte surface binding and activating Nogo Receptor on a neuron. 18 However, doubts have emerged as to the plausibility of RTN4 transducing signals through cell-to-cell (oligodendrocyte-to-neuron) contact. Namely, RTN4's



²Department of Zoology, Cambridge, UK

³Department of Neuroscience Biomedicine and Movement Sciences, University of Verona, Verona, Italy

⁴Department of Physics, University of California, San Diego, 9500 Gilman Dr. #0374, La Jolla, CA 92093-0374, USA

⁵Department of Physics, Toronto Metropolitan University, Toronto, ON M5B 2K3, Canada

⁶Department of Physics, Harvard University, Cambridge, MA 02138, USA

⁷Cambridge Institute for Medical Research (CIMR), Department of Medicine, University of Cambridge, The Keith Peters Building, Hills Road, Cambridge CB2 0XY, UK

⁸Department of Chemistry and Biochemistry, Calvin University, Grand Rapids, MI 49546, USA

⁹Wellcome-MRC Cambridge Stem Cell Institute Advanced Imaging Facility, Puddicombe Way, Cambridge CB2 0AW, UK

¹⁰Lead contact

^{*}Correspondence: ekoslover@physics.ucsd.edu (E.F.K.), ea347@cam.ac.uk (E.A.) https://doi.org/10.1016/j.celrep.2024.114357



membrane topology appears to be incompatible with this model, as its reticulon homology domain (RHD) was later shown to embed in the outer surface of the ER membrane, in a double hairpin form. This configuration precludes the exposure of any moieties to the ER lumen/outer cell space. Further, RTN4 was observed to localize exclusively to the ER in multiple cell lines. These observations lead us to hypothesize that RTN4's Nogo effect is mediated specifically through the ER, raising the question of how an ER morphogen can determine neurite outgrowth.

To test this hypothesis, we first sought to establish whether ER-localized RTN4 is necessary and sufficient to trigger the Nogo effect and, if so, to provide a plausible mechanistic explanation for this phenomenon by delineating the effects of RTN4 on ER structure and function. Our measurements demonstrated that the Nogo effect of RTN4 in human cortical neurons is directly mediated by the ER. Further, we established that RTN4 modulates ER morphology by constricting or expanding luminal space (using CRISPR-Cas9 KO and controlled exogenous expression).

Using a purpose-developed quantitative analysis of photoactivated protein spreading, together with mathematical modeling of network transport, we demonstrated that the morphoregulatory effect of RTN4 controls luminal transport rates, thereby altering Ca²⁺ supply for physiological release events. Thus, our results provide a mechanistic link between the RTN4-regulated architecture of the ER, its function as an intracellular transport system, and the modulation of neurite outgrowth via the Nogo effect.

RESULTS

ER-localized RTN4 inhibits neurite outgrowth

Though the role for ER morphological regulation in neuronal health and function is suggested by the genetic and biochemical association of ER morphogens with neurodegenerative diseases, ^{6,8,9} the nature of this link remains obscure. We postulated that the observed effect of a known ER morphogen (RTN4/Nogo) on neurite outgrowth has the potential to elucidate the role of ER morphoregulation in neuronal health and function. However, drawing such connections requires confirmation that the Nogo effect is indeed mediated specifically by ER-localized RTN4 in neurons. In particular, as the neurite outgrowth-inhibiting effect of RTN4 has been demonstrated only in whole-organism models, 11,12 three critical aspects of the phenomenon remained inaccessible: (1) the presence of the Nogo effect in human neurons, (2) whether the effect is mediated by RTN4 within the neurons or from the surface of the contacting neuroglia, and (3) whether the effect is associated specifically with ER-localized RTN4 and can be attributed to the ER morphoregulatory functions of this protein. To address these questions, we assessed the effects of RTN4 manipulations in cortical neuronal monocultures (oligodendrocyte-free) derived from human induced pluripotent stem cells (hiPSCs;²²; Figure 1A). The neuronal cultures can be matured to a neuro-physiologically active state, reflected by the cells' synchronous Ca2+ firing (Video S1; Figure S1). Immunofluorescence with high-resolution microscopy revealed a typical reticulated ER pattern of endogenous RTN4 in neurites (Figure 1B), and the fluorescence signal of HaloTag-fused RTN4a was distinguishable from that of a plasma membrane marker (Figure 1C).

Conspicuously, the stably overexpressed RTN4 inhibited neurite outgrowth (Figures 1D, S2, and S3; Video S2). Moreover, most transiently RTN4-overexpressing cells failed to generate neurites during neuronal differentiation (Figure 1E). This effect is not explainable by RTN4 cytotoxicity, as the overexpressed protein was readily detectable, revealing soma of transfected cells at all times. RTN4 was also visible in the apparently underdeveloped (compared to untransfected) neurites appearing with a severe delay (Figure 1E, day 7). Further, neurons not undergoing plasticity events tolerated RTN4 in their neurites' ER when overexpression was imposed post differentiation (Figure 1F).

To confirm the neurite outgrowth-enhancing effect of RTN4 elimination observed in vivo, we generated a mutant iPSC neuronal progenitor line with constitutive loss of function for RTN4 by genome-editing its locus using CRISPR-Cas9. We selected lines with homozygous frameshift mutations and validated the loss of expression on the protein level by immunoblot (Figure S4A). Consistent with the viability of RTN4 KO animals, its loss in human neurons showed no apparent phenotypic disadvantage, and in agreement with observations in vivo, RTN4 KO improved neuronal outgrowth during iPSC differentiation (Figures 1D, S2, and S3A) with no effect on total cell mass (Figure S3B). Further, we assessed the neurite outgrowth rate following a localized mechanically inflicted injury of the neuronal networks by tracing their elongation in automated phasecontrast imaging (Figure 1G; Video S3). This assay showed a significant increase in the elongation rate of RTN4 KO cells compared to the isogenic wild type (WT) (Figure 1H).

Thus, the measurements of hiPSC-derived cortical neuron (iNeuron) neurite generation and RTN4's ER-exclusive localization point to an intracellular Nogo effect of RTN4, originating from the ER and confirm its relevance to human neurons.

RTN4 load defines ER tubular width

To assess the effect of RTN4 on tubular ER ultra-structure, we visualized the endogenous RTN4 in sub-diffraction resolution along with an ER luminal marker (Figure 2A). The images showed a heterogeneous distribution of the protein across the ER network (Figure 2A; Video S4). Notably, the RTN4-enriched tubular areas showed a profound reduction in the luminal marker's signal (Figure 2A; Video S4), which was more obvious at the peripheral region compared to the perinuclear region. The luminal content exclusion by endogenous RTN4 was observed in two super-resolution modalities: lattice structured illumination microscopy (lattice-SIM; Figure 2A) and Lightning deconvolution laser scanning microscopy (Video S4), and was further emphasized by exogenously overexpressed RTN4 (Figure 2B). These observations agree with electron microscopy (EM) data²³ and suggest that this morphogen may constrict the ER luminal space (Figures 2A and 2B). This idea is supported by the fact that RTN4's RHD, responsible for its ER membrane localization, assumes a wedge-like configuration that can impose curvature on the tubule membrane. 1,24 Overexpression of an RTN4 splice variant with an identical RHD and lacking a cytoplasmic extension, RTN4c, also resulted in significant luminal marker exclusion (Figure 2B). Consistently, another reticulon (RTN2) showed a similar effect when overexpressed,²⁵ while RTN3 seems to contribute to ER morphoregulation

Article



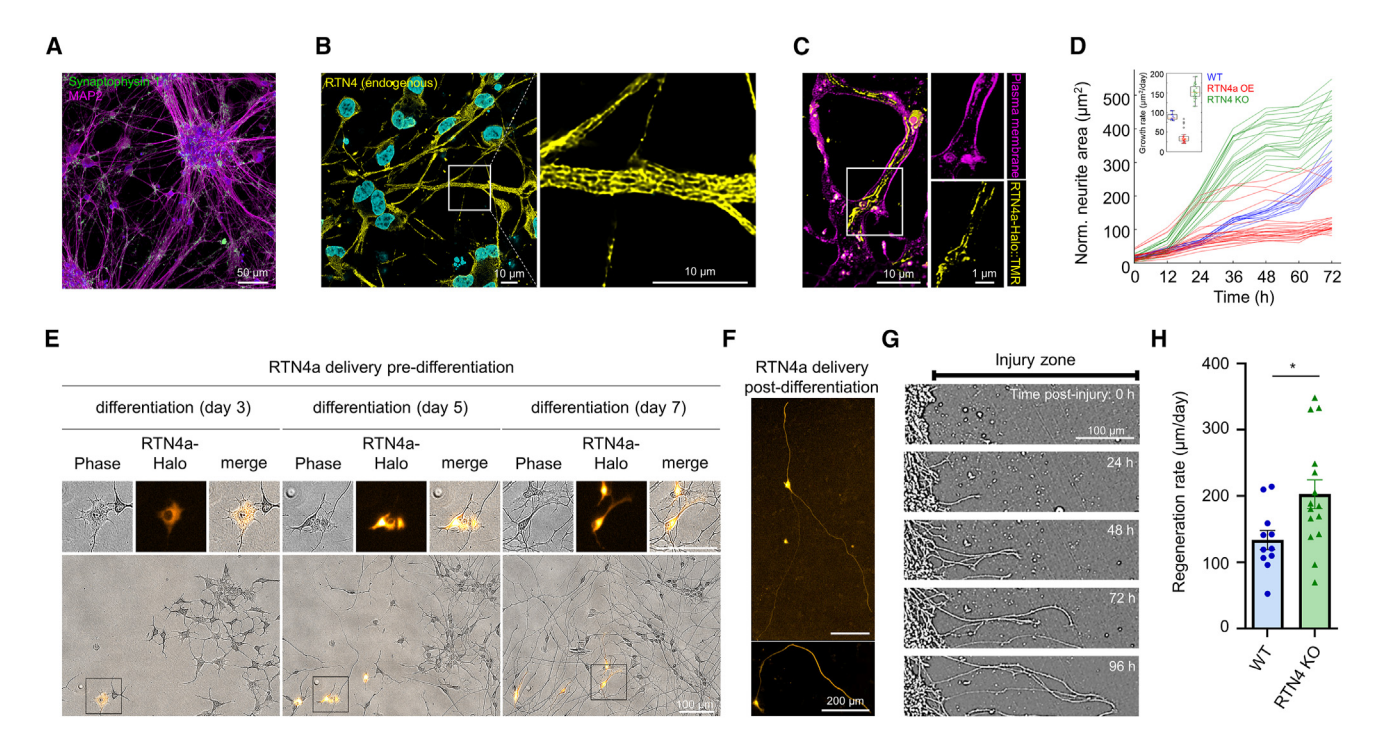


Figure 1. RTN4 hinders neuronal outgrowth/regeneration in human iPSC-derived cortical neurons

(A) Representative image of differentiated human iPSC-derived cortical neurons (iNeurons; day 21) stained by synaptophysin 1 (green, a presynaptic vesicle marker), microtubule-associated protein 2 (MAP2; magenta, a neuronal marker), and Hoechst 33258 (blue, a nucleus label).

(B and C) Micrographs of (B) immunolabeled endogenous RTN4 in fixed iNeurons (day 21) with sub-diffraction-limit resolution and (C) of exogenous RTN4a (RTN4a-Halo::TMR, yellow) co-stained with a plasma membrane marker (Cellbright, magenta).

- (D) Normalized area covered by neurites during outgrowth of the WT and a pool of stably RTN4a-overexpressing (OE) or RTN4 knockout (KO) iNeurons. Inset: corresponding growth rate extracted from a linear fit. Note the extensive stable RTN4a-Halo expression throughout RTN4a OE iNeurons. See also Figure S3C. (E and F) Micrographs of iNeurons with exogenously introduced RTN4a-Halo (J646 labeled, orange) at the indicated differentiation stage.
- (E) Lentiviral particles of RTN4a-Halo were introduced 48 h pre differentiation (shown are images from differentiation days 3, 5, and 7 in the same field).
- (F) As in (E), but RTN4a-Halo was introduced post differentiation (day 14). Note the compromised neurite outgrowth in RTN4a-OE cells and detectable distribution of RTN4a in neurites when iNeurons possess neurites.
- (G) Representative time-lapse images of neurite regeneration following a mechanical injury.
- (H) Neurite regeneration rate in WT and RTN4 KO iNeurons.

Shown are means \pm SEM from three independent experiments. *p < 0.05 (Student's t test).

differently. ^{13,26} Thus, the functional specificity and redundancy of distinct reticulon-family proteins are currently ambiguous.

To test whether and to what extent RTN4 can modulate ER tubular width, we sought to measure its changes in response to RTN4 overexpression and KO. The scale of the ER tubule cross-section (<100 nm²⁷) is below the resolution limit of light microscopy. To surmount this limitation, we extract the tubular width by analyzing fluorescence intensities of an ER membrane marker, a technique compatible with live-cell imaging. Our approach draws on the principle that the membrane marker signal intensity on a cylindrical structure (i.e., the ER tubule) is proportional to its radius, while the intensity on a flat structure (the ER sheet) depends only on its area (see STAR Methods for details). Thus, the tube radius R was approximated by Equation 1:

$$R = AI_{\text{tube}} / (\pi L I_{\text{sheet}})$$
 (Equation 1)

where I_{sheet} is signal intensity on a peripheral sheet segment of area A and I_{tube} the intensity along nearby tubule segments of length L. We note that the tube length L and sheet area A corre-

spond to selected segments and thus do not depend on the total extent of tubular and sheet-like ER structures in the cell. Consistently, ER sheet expansion through CLIMP63 overexpression did not affect the estimates of tube radii (Figure S5).²³

This measurement yielded similar values in live and fixed cells (R = 53.3 ± 8.3 and 51.0 ± 7.6 nm, respectively), suggesting that our fixation protocol did not alter ER architecture (Figure S6). These values were also consistent, both in terms of average and variance, with previous estimates from super-resolution imaging studies (diameter, 96 \pm 17 nm²¹). The broad spread of the measurements may reflect, in addition to a natural tubule variability, potential inaccuracies resulting from morphological heterogeneity of the peripheral sheets. Past work indicated that some apparent peripheral sheets are composed of dense tubular matrices (observed by SIM28) or hole-studded perforated sheet structures (observed by stimulated emission depletion microscopy²¹). Such alternate structures for the peripheral sheets would lead to an overestimate of the tube radius, and an underestimate of the change in radius associated with morphogen expression perturbations (see Figure S7 and



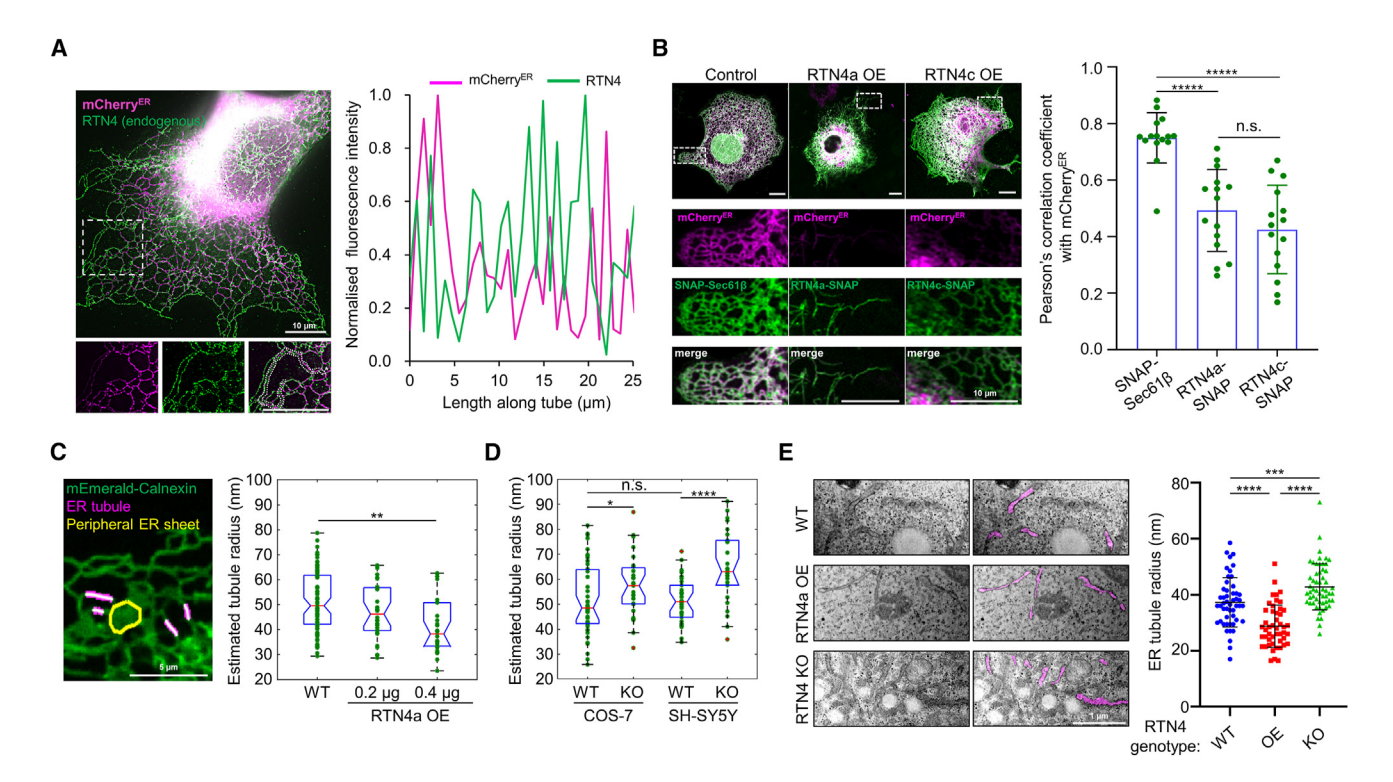


Figure 2. RTN4 narrows ER tubules

(A) Fluorescence micrographs of endogenous RTN4 (immunolabeled, green) and an exogenously expressed ER luminal marker (mCherry^{ER}, magenta) in fixed COS-7 cells, shown along with a line-scan analysis of the fluorescence intensity along peripheral ER tubules (dashed line in the inset).

(B) Colocalization analysis of the ER luminal marker (mCherry^{ER}) vs. overexpressed ER membrane proteins (SNAP-Sec61 β , RTN4a-SNAP, or RTN4c-SNAP) (n = 15). Note decreased colocalization in RTN4 overexpression, reflecting luminal exclusion (Pearson correlation coefficients, mean \pm SD, SNAP-Sec61 β : 0.750 \pm 0.089, RTN4a-SNAP: 0.493 \pm 0.145, RTN4c-SNAP; 0.425 \pm 0.157). Note the incomplete colocalization observed in SNAP-Sec61 β -OE cells due to endogenous RTN4 anisotropic distribution, as shown in (A).

(C) A representative micrograph with ER tubules and sheets used for ER radius estimation in COS-7 WT (51.3 \pm 11.6 nm) and RTN4a-OE cells (0.2 μ g; 47.2 \pm 10.9 nm, 0.4 μ g; 41.4 \pm 11.1 nm). Note a decrease of the ER tubule radius with increasing amounts of RTN4a.

(D) Measurements as in (C) of COS-7 WT (51.7 \pm 14.0 nm) and RTN4 KO (57.5 \pm 12.4 nm) and SH-SY5Y WT (51.4 \pm 9.0 nm) and RTN4 KO (65.0 \pm 14.5 nm) cells. COS-7 WT, n = 47; COS-7 RTN4 KO, n = 26; SH-SY5Y WT, n = 30; SH-SY5Y RTN4 KO, n = 26.

(C and D) The values are means ± SD. Note that two ER membrane markers, calnexin and Sec61β, yield the same values for WT samples.

(E) Representative TEM images (left) were segmented. ER tubules are depicted in magenta (right). Measured ER tubule radius is shown for COS-7 WT (37.3 ± 8.8 nm, n = 50), RTN4a-OE (28.8 ± 7.5 nm, n = 48), and RTN4 KO (42.8 ± 8.2 nm, n = 56) cells.

The values are means \pm SD. *p < 0.05, **p < 0.01, ***p < 0.005, ****p < 0.001; n.s., not significant.

STAR Methods for a detailed analysis of how perforated sheets or tubule matrix structures affect the radius estimates). Notably, the most recent focused ion beam scanning EM 3D reconstructions from cryo-preserved cells (an approach presumably free from optical artifacts) showed the presence of smooth peripheral ER sheets. ²⁹ Thus, we expected that the intensity-based assessment of tubule dimensions can detect changes arising from RTN4 manipulations in fixed or unperturbed cells.

By comparing relative radius estimates under different conditions, our measurements confirmed a dose-dependent narrowing of the ER tubules by exogenous RTN4 (Figures 2C and S8). Remarkably, endogenous levels of RTN4 also constrict tubules, as evident from a measurable increase in tubule width upon elimination of RTN4 expression by CRISPR-Cas9 KO in COS-7 cells and in a human neuroblastoma (SH-SY5Y) cell line (Figures 2D, S4B, S4C, and S8; KO cell lines generated as in Figure 1). These findings are consistent with a previous

report using embryonic fibroblasts of an RTN4 KO mouse.³⁰ Notably, eliminating RTN4 from SH-SY5Y led to a more conspicuous increase in tubule width, suggesting that the endogenous RTN4 burden might be higher in this cell line compared to that of COS-7 cells (Figure 2D). Further, transmission EM (TEM) measurements confirmed the tubule-narrowing effect of RTN4 overexpression and the tubule dilation upon its KO (Figure 2E). The values obtained by EM measurements were comparable with fluorescence-based estimations, with a slight shift toward lower values (Figures 2C–2E and S6), consistent with membrane compaction due to dehydration during EM sample preparation, as reported previously.²¹

ER tubule narrowing affects the kinetics of luminal transport

We hypothesized that the observed alteration of ER tubular width by RTN4 may modulate luminal content transport through the ER



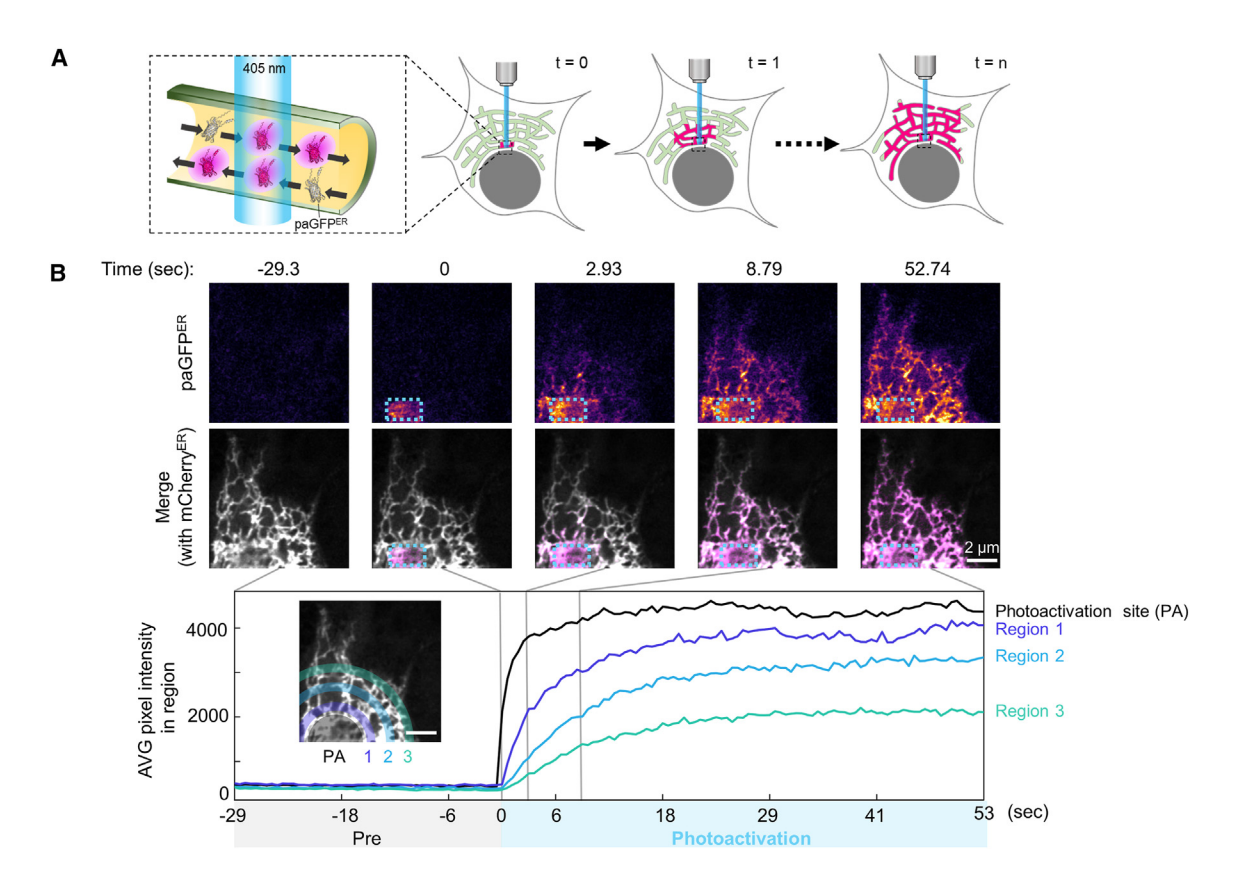


Figure 3. Establishment of the CPAC assay

(A) Schematic of the CPAC assay. ER-targeted photoactivatable GFP (paGFP^{ER}) restores its fluorescence characteristic as conventional GFP by 405-nm laser irradiation. Photoactivated paGFP^{ER} is continuously supplied at the photoactivation site during the photoactivation period, and transport of the molecules throughout the ER is monitored over time.

(B) Empirical demonstration of the assay. Locally photoactivated paGFP^{ER} at the perinuclear region is transported along the ER luminal marker (mCherry^{ER}) over time. Average (AVG) pixel intensity of paGFP^{ER} was measured at respective ROIs with different distances from the photoactivation spot.

network and, consequently, control the rate of material exchange across long cellular distances. In addition to lower volumes of material delivered by narrow tubules, putative flows within the ER lumen³¹ could also be reduced by tubule narrowing, as expected for a microfluidic pipe.³² To test this hypothesis, we established a measurement technique for intra-organelle transport relying on spatiotemporal signal profiling in response to continuous photoactivation of a tracer at a fixed position (continuous photoactivation chase [CPAC]; Figure 3). By tracing the signal arrival times at increasing distances from a point of continuous optical injection of a photoactivatable fluorescent protein,³³ this approach can reveal the mode of molecular transport and its kinetic parameters.

To extract quantitative measurements of transport from the signal arrival times, we compared the CPAC results to simulations of particle transport over a network. Namely, we used a continuum model to solve the time evolution of the concentration profile of photoactivated particles over a synthetic network structure (Figure 4A; Video S5). The concentration was held fixed within a circular region representing the photoactivated zone, and the simulations were carried out in a hexagonal network embedded within a domain shape extracted from images of the background ER signal. With these boundary conditions, the diffusion equation

was solved numerically using a finite volume method to obtain concentration profiles over time. These profiles were augmented with synthetic noise and analyzed in a manner analogous to experimental images.

We quantified the signal over time in individual wedge-shaped regions at increasing distances from the photoactivated center and extracted a half-time for signal rise in each region (Figure 4A, right). For each distance, the half-times were averaged over many wedge regions from multiple cell geometries. As expected, the resulting half-times scale quadratically with distance (Figure 4B, red curve). The simulations were then expanded to include active flows along the network tubules. Crucially, this resulted in more rapid signal arrival at large distances from the photoactivated site, altering the scaling of the signal half-times with distance (Figure 4B, blue curve; note that the presence of adjacent sheets or a nuclear envelope reservoir does not significantly alter the kinetics of signal arrival into tubular regions; Figure S9). Thus, the distance-dependent arrival curves of CPAC can be used to distinguish between diffusive and effectively superdiffusive motion.

Next, we analyzed the experimental CPAC images in the same manner as simulated data (Figures 4C and 4D). In agreement with simulations, measurement of the signal spread kinetics for an ER membrane marker showed diffusive scaling (Figure 4D,



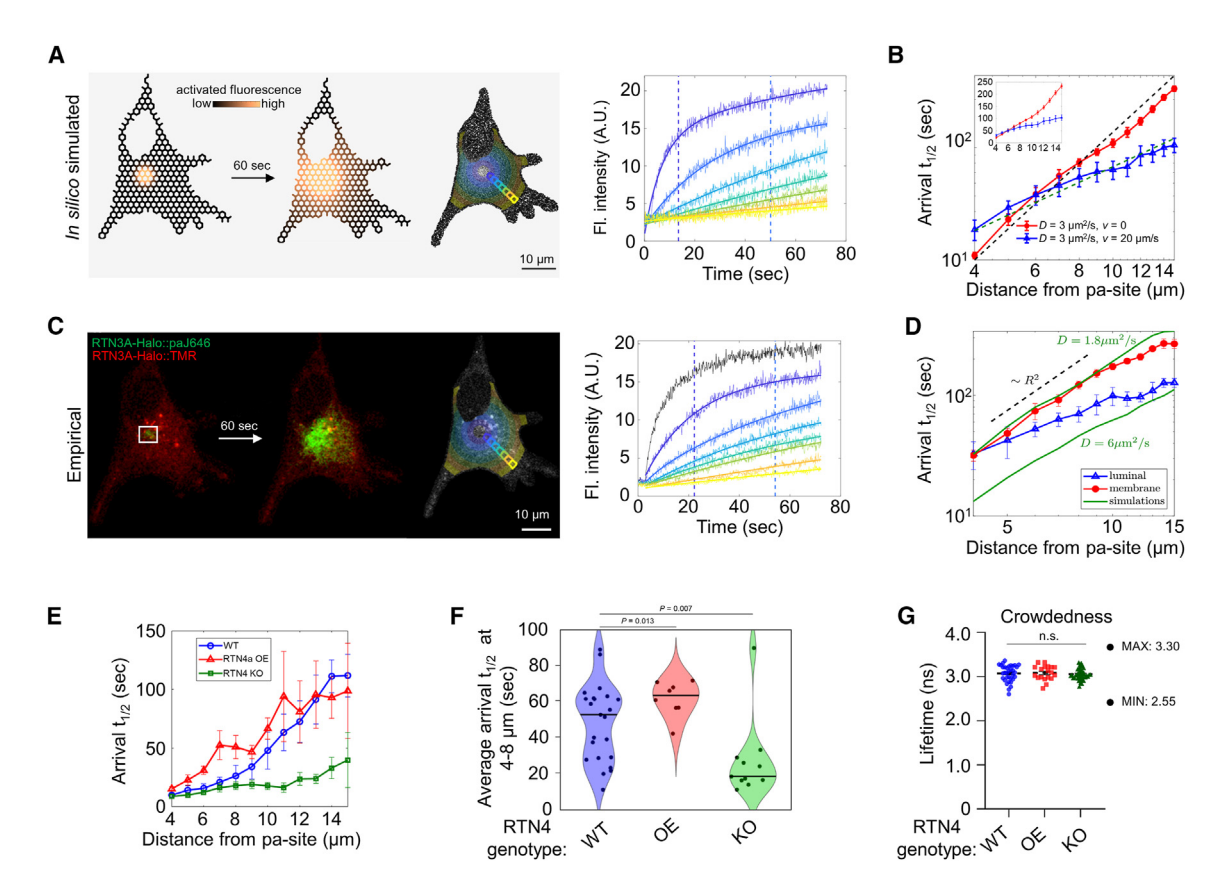


Figure 4. ER morphoregulation by RTN4 modulates ER luminal transport rates

(A) Simulations of spreading from a continuously photoactivated region on a regular lattice of tubules in a cellular geometry. The rightmost image shows a concentration profile with added synthetic noise, analyzed as for experimental CPAC data. Rings at different distances from the photoactivated region are shown in transparent color. Example wedge regions used to track signal intensity are shown for each ring. The plot shows simulated noisy signal intensity over time in each of the wedge regions (matching color). Vertical dashed lines indicate the arrival half-time (t_{1/2}) for the two nearest regions.

(B) Simulated median arrival $t_{1/2}$ averaged over all regions at a given distance from the photoactivated center in cell geometries (n = 8). Concentration profiles spread by diffusion alone (red) are compared against those on an active network with randomly oriented flows in each edge (blue), of velocity $v = 20 \mu m/s$, and persisting over $\tau = 0.1$ s. Results are plotted on log-log axes to emphasize scaling behavior (black dashed line, $t_{1/2} \sim R^2$; green dashed line, $t_{1/2} \sim R$ shown as guides to the eye). Note that active flows result in a super-diffusive (sub-quadratic) scaling of signal arrival times versus distance. Inset: the same plot on linear axes. Error bars show standard deviation of the median, obtained by bootstrapping at the level of individual simulated cells.

(C) Representative images of continuous photoactivation chase (CPAC) in COS-7 cells transiently expressing RTN3A-HaloTag (RTN3A-Halo) labeled by tetramethyl rhodamine (50 nM, 2 h) and photoactivatable-Janelia Fluor 646 (paJ646; 200 nM, 2 h). A white box denotes the area of paJ646 photoactivation by laser illumination (405 nm). Traces of photoactivated signal intensity are shown for each of the marked wedge regions.

(D) Median half-time of photoactivated signal rise (arrival $t_{1/2}$, exemplified by vertical dashed lines in (C) for paGFP^{ER} (blue) or an ER membrane marker (RTN3A-Halo::paJ646, red) at various distances from the activation spot. Note that measurements for membrane protein are well matched by simulations of diffusive spread with D = 1.8 μ m²/s. Luminal protein measurements show transport with super-diffusional scaling and cannot be fit by higher diffusion coefficients (compared to simulations up to D = 6 μ m²/s, green lines).

(E and F) paGFP^{ER} arrival t_{1/2} measurements as in (D) in mCherry^{ER} (control, RTN4 KO) or mCherry-RTN4a OE (RTN4 OE) COS-7 cells (n = 15 each) (E) and in SH-SY5Y cells (F; P derived from Kolmogorov-Smirnov test). Bars in (F) indicate median.

(G) Fluorescence lifetime imaging microscopy (FLIM) measurements of an ER-localized molecular crowding probe in cells as in (F) (n = 34, 19, and 42, respectively).

red curve). ER membrane proteins exhibited the same diffusive behavior regardless of their topology, as both a monotopic membrane protein, RTN3A-Halo, and a transmembrane protein, Sec61 β , demonstrated quadratic scaling with similar rate values (Figure S11). The estimated diffusivity for RTN3A-Halo from our CPAC data is roughly consistent with prior measurements of ER membrane protein diffusivities.³⁴

The signal half-times for the luminal protein exhibit a superdiffusive scaling that cannot be fit by simply increasing the diffusion coefficient (Figure 4D, blue curve). This observation is consistent with an active component contributing to ER luminal transport.³¹ The marked difference in behavior of luminal vs. membrane markers argues against the possibility of superdiffusive behavior resulting from membrane dynamics driven by cytoskeletal rearrangements. Furthermore, the diffusive scaling observed for membrane proteins indicates that details of the tubular network structure itself are unlikely to account for the superdiffusive spreading of luminal proteins.

Article



Notably, the signal from ER-targeted photoactivatable GFP (paGFP^{ER}) outside the illumination region showed fluctuations in intensity suggesting a pulsatile pattern of spread across the network (Video S6). Although the mechanism of flow generation in the ER remains to be established, this observation may support a pumping-like effect of contraction and relaxation of ER structure elements (tubules, sheets, or junctions).³¹

These measurements demonstrated that the CPAC methodology provides a sensitive means to quantify transport behavior across a range of cellular distances. Therefore, we applied CPAC to characterize how RTN4-mediated ER tubule narrowing affects transport rates throughout the ER.

CPAC analysis revealed that overexpression of RTN4 slowed down the arrival of locally photoactivated paGFP^{ER} at increasing distances (Figures 4E, 4F, and S10B; automated and manual analyses, respectively). In contrast, RTN4 KO cells showed a conspicuous increase in protein mobility through the ER network, as reflected by faster arrival of photoactivated luminal signal at distant regions (Figures 4E, 4F, and S10C). Thus, the changes in protein mobility, observed upon manipulations of RTN4 expression, mirror their tubule width-modulating effect; RTN4imposed narrowing of ER tubules correlates with slower luminal material transport, while tubule widening in RTN4 KO appears to improve material exchange across the ER network. This is further supported by the capacity of another ER morphogenic protein, RTN2C, to compensate for RTN4 deficiency; its expression leads to tubule narrowing, as evident from luminal exclusion and restoration of tubule caliber in RTN4 KO cells (Figures S12A and S12B). Consequently, the RTN2C was able to reverse the difference in luminal mobility of RTN4 KO cells (Figure S12C). RTN4 manipulation did not cause detectable alterations in luminal crowdedness (Figures 4G and S13). It should be noted that a simple decrease in tubule radius, without modulating transport velocities, would merely rescale the fluorescence intensity measurements throughout the network and would not be expected to alter photoactivated signal rise times. Thus, the effects seen here provide direct evidence of altered transport speed, in addition to changes in volumetric flow rate, associated with modulation of tubule radius.

One plausible mechanism for coupling ER tubule width with spatial transport rates could be modulation of active luminal flows, consistent with the observed superdiffusive spreading of luminal proteins (Figure 4D). The classic Poiseuille flow model for pressure-driven motion of a viscous fluid through a narrow tube predicts that the flow speed v scales with radius R according to $v \sim R^2$. Furthermore, a lower radius could reduce the persistence time of flows that result from tubule contraction. Alternate explanations are also possible, including variation in channel width along individual tubules, which may result in local constrictions that block or severely restrict transport routes upon RTN4 overexpression.

ER morphoregulation by RTN4 modulates Ca²⁺ release capacity

Next, we set out to examine the consequences of transport speed modulation on ER function as a Ca^{2+} delivery system. This ER activity controls cell regeneration; an adequate supply of Ca^{2+} is required for the ER-powered release of this messenger ion at neu-

rite growth cones. Local Ca²⁺ transients trigger outgrowth and define its direction.^{35,36} We sought to assess how ER morphore-gulation modulates its performance as a Ca²⁺ storage and supply system. To this end, we accessed key relevant parameters of Ca²⁺ homeostasis: (1) the intensity of transient cytoplasmic Ca²⁺ elevations in optogenetic ER releases and (2) ER luminal steady state concentrations, implementing optical probes suitable for each measurement, as described below.

The measurements were conducted following theoretical exploration of how intra-luminal transport and ER morphore-gulation might affect local calcium release dynamics. Namely, RTN4 overexpression was expected to reduce Ca²⁺ delivery within the ER through two complementary effects: the reduced flux arising directly from a diminished cross-sectional area and the reduced long-distance transport speeds as observed in CPAC measurements (Figure 4). This was supported by a physical simulation of Ca²⁺ transport across the ER network and its ability to supply local releases (Figure 5A; Video S7), using a continuum model that incorporated buffer binding, ER network structure, intra-luminal transport, and local permeability.³⁷

Estimates from published measurements of Ca²⁺ release currents (see STAR Methods for details) indicate that the effective permeability due to open channels in the ER membrane is sufficiently high to locally deplete the releasing region of the ER and to necessitate transport of Ca²⁺ from elsewhere in the lumen.³⁷ Our simulations included both diffusive and active dynamics to numerically evolve the spatiotemporal concentration profiles of free Ca²⁺ and buffer proteins on a realistic ER network structure under the assumption of rapid binding equilibration (see STAR Methods for details). Buffer binding was found to provide an important connection between putative reduced flows due to tubule narrowing and ion transport.³⁷ Because larger buffer proteins diffuse much slower than calcium ions, their transport is more dependent on active luminal motion over and above diffusion.

Starting with a homogeneous concentration profile for both buffer sites and ions, we tracked the flux of Ca2+ leaking out of the network within a local permeable region (Figure 5A, red curve). These simulations predicted that narrower tubules would reduce Ca²⁺ release (Figure 5A, magenta curve) by decreasing the available luminal volume. Furthermore, tubule narrowing is expected to reduce the flow velocity in the lumen, as evidenced by the slower spreading of the photoactivated marker in CPAC measurements upon RTN4 overexpression (Figures 4E and 4F). However, the extent of this reduction is unknown. We therefore considered the limiting case of halting the flow (transport of ions and buffer proteins was reduced to purely diffusive motion; Figure 5A, blue curve). A further reduction in Ca²⁺ release under these conditions indicated that Ca2+ release-capacity can be modulated both directly by changes in tubule width (reducing surface area and total quantity of Ca2+ in the local release region) and by the concomitant attenuation of active transport (reducing the replenishment of depleted local calcium). Notably, transport effects are expected to modulate Ca²⁺ release on timescales above \sim 1 s (Figure 5A). Sub-second events correspond to the release of locally stored calcium within the permeable region, while longer timescales require long-range transport through the ER lumen.



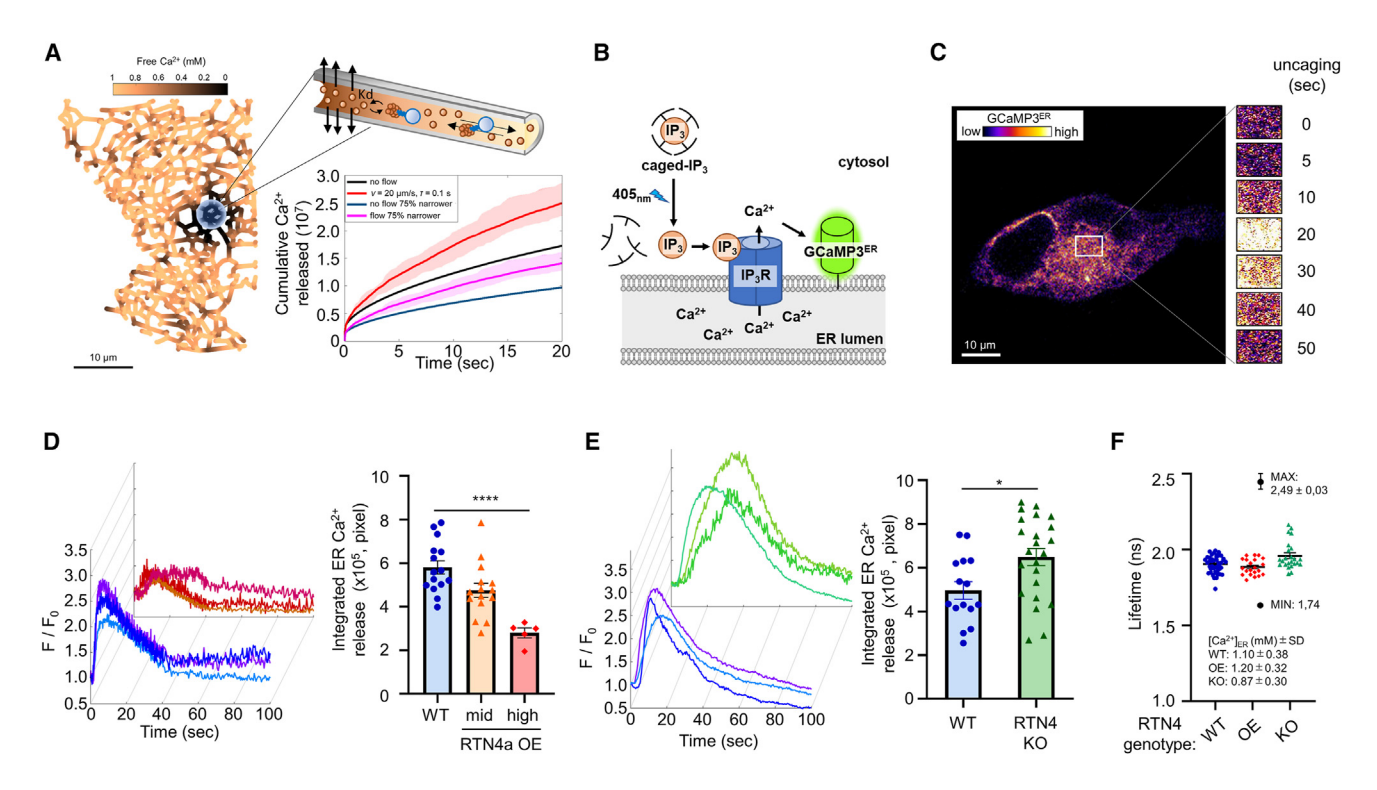


Figure 5. RTN4 ER morphoregulatory/transport effect curbs ER Ca²⁺ release capacity

(A) Physical simulation of the dependence between ER Ca^{2+} release capacity and luminal transport, incorporating equilibrated binding to Ca^{2+} buffer proteins, local ER release, diffusive luminal transport of free/buffered Ca^{2+} , and luminal flow, with plots of total Ca^{2+} released over time. Note that release capacity decreases both as a result of halting active flows and from the direct decrease in flow rate due to tubule narrowing.

- (B) Schematic of light-induced ER Ca²⁺ release and monitoring assay.
- (C) Representative fluorescence intensity image series of GCaMP3^{ER} at photo-uncaging regions of COS-7 cells preloaded with caged IP₃ (3 μM, 3 h, uncaging by continuous 405-nm laser illumination).
- (D) Traces of GCaMP3^{ER} signal as in (C) in WT or RTN4a-OE SH-SY5Y cells, shown along with the integrated ER Ca²⁺ released during the uncaging period (the area under the curve; WT, n = 17; RTN4a OE, n = 20). Shown are means \pm SEM from samples in three independent experiments. ****p < 0.001 (one-way ANOVA). (E) As in (D) for WT and RTN4 KO SH-SY5Y cells (WT, n = 15; RTN4 KO, n = 23). *p < 0.05 (Student's t test).
- (D and E) Note the equivalent dynamic range in the WT.
- (F) FLIM measurements of ER Ca²⁺ using the D4ER probe in cells as in (D) and (E). Note that the lifetime is inversely proportional to [Ca²⁺]_{ER}.

These predictions were tested by mimicking physiological Ca²⁺ release from the ER, using local photolysis of caged inositol trisphosphate (IP₃). IP₃ is generated in natural signaling (including in outgrowth) as a transient second messenger that triggers ER Ca²⁺ release by binding an ER membrane Ca²⁺ channel—the IP₃ receptor. ^{38,39} ER Ca²⁺ efflux triggered by uncaged IP₃ was monitored by a cytoplasmic Ca²⁺ sensor tethered to the ER membrane (GCaMP3^{ER}; Figures 5B and 5C). Measurements in this modality demonstrated that ER Ca²⁺ release was dampened by RTN4 overexpression compared to WT cells (Figure 5D; amount of Ca²⁺ release reflected in the area under the curve). In contrast, RTN4 KO cells showed a measurably more robust release capacity (Figure 5E).

To assess whether this observation reflects RTN4's effect on ER Ca²⁺ content, we exploited a fluorescence lifetime-based method that allows measuring absolute Ca²⁺ concentration in the ER lumen in a calibrated manner, with an estimated sensitivity that allows detecting changes of $\pm 10\%.^{40,41}$ We observed a slight deviation (on the border of significance) in free Ca²⁺ for KO and RTN4-overexpressing cells compared to the WT (Figures 5F and S14). This de-

viation was in the opposite direction from the effect of these genotypes on Ca²⁺ release. Therefore, alterations in intra-ER Ca²⁺ are not responsible for the RTN4-associated changes in its release.

The RTN4-dependent changes in the ER's ability to release Ca^{2+} mirror the effect of this morphogen on ER luminal width and transport (Figures 2 and 4). As expected from simulations (Figure 5A), RTN4-mediated narrowing of ER tubules led to weakened Ca^{2+} releases, while eliminating the endogenous morphogen increases luminal mobility and strengthens Ca^{2+} peaks. Given current measurement techniques, it is not possible to disentangle how much of this modulation in release is caused directly by decreased luminal volume and how much is associated with the reduction in luminal mobility. However, our simulation results indicate that both effects are expected to contribute to the RTN4-mediated reduction in Ca^{2+} release.

DISCUSSION

The current findings establish a link between ER morpho-regulation and its performance as a luminal content delivery system



with consequences for neuron outgrowth and regeneration. We circumvented the limitations of real-time molecular transport measurements by developing an approach (CPAC) to measure the spatiotemporal distribution of ER contents through continuous local photoactivation coupled to signal tracking in spatially distributed regions. These measurements, combined with physical modeling of diffusive and advective transport within a tubular network, enable quantification of the transport behavior of ER luminal proteins. We show that the motion of luminal contents is consistent with active flows within individual tubules and that the long-range spreading is hindered by tubule narrowing associated with RTN4 overexpression. Furthermore, we demonstrate that RTN4 modulates localized calcium release from the ER and leverage simulations to demonstrate that such modulation can be explained by changes in both tubule radius and transport rates.

Taken together, these findings indicate that ER morphore-gulation can modulate material distribution throughout the cell periphery, tuning Ca²⁺ release profiles. The endogenous level of RTN4 expression is sufficient to substantially constrain ER transport, as RTN4 KO leads to improved transport kinetics (Figures 4E and 4F) and augmented Ca²⁺ release (Figure 5E).

Given the crucial role of ER Ca²⁺ release at the leading edge of outgrowing/regenerating cellular projections, including neurites, 36 the role of RTN4 in this process may explain the puzzling plasticity-restricting (Nogo) effect of this gene. The Nogo effect of excess RTN4^{15,17} and, conversely, the enhancement of axonal regeneration upon RTN4 elimination is reproduced in vivo 11,12,16,42 and confirmed in Figure 1. This phenomenon was initially attributed to a cell-surface subpopulation of the reticulon in oligodendrocytes, activating an outgrowth-inhibiting Nogo receptor on the neurons' surface. 18 However, extracellular antibody-mediated targeting of RTN4 proved inefficient in clinical trials. 43 Later studies indicated that RTN4 assumes a membrane topology prohibiting extracellular/ER luminal exposure of the protein segments to interact with the Nogo receptor.44 Though this explains the lack of effect from the cellimpermeable antibody, the mystery of how an ER morphogen can limit axonogenesis acting from within the ER remained unresolved. The above findings on RTN4's role in ER morphoregulation and, consequently, Ca2+ supply offer a solution to this paradox. Namely, we propose that RTN4-mediated narrowing of the ER tubules hinders the long-range transport and delivery of luminal material. This results in attenuation of the ER's capacity to fuel Ca2+ releases (crucial for axonal growth) and may limit neurite outgrowth as well as axonal plasticity and

Thus, the consequence of ER morphoregulation by RTN4 for the modulation of neurite plasticity provides a direct link between ER structure and its function as an intracellular delivery system, relevant for axonogenesis. The high expression of RTN4 in the central nervous system may also contribute to its stable suppression or regenerative plasticity. Given the tolerance of RTN4 KO in cultured neuronal networks (Figure 1) and on the organismal level 12,42 with no apparent phenotypical disadvantages, targeting RTN4 intracellularly might constitute a viable therapeutic strategy to enhance axonogenesis.

Limitations of the study

Our study demonstrates that overexpression of RTN4 narrows ER tubules and concomitantly reduces the rates of luminal transport across the peripheral network. One possible explanation for decreased spatial transport is that narrowing tubules reduces the stochastic luminal flows which have been reported previously in the ER.31 Our quantitative analysis of CPAC data, coupled with numerical simulations, further substantiates the non-diffusive spreading of luminal material and indicates that the observed effects are consistent with reduction in luminal flow. However, other explanations could also account for the relationship between tubule width and spatial dispersal rates. For example, a non-uniform width of the ER tubules could give rise to local constrictions, 45 which become fully blocked upon accumulation of excess RTN4, thereby increasing the tortuosity of the paths particles must follow to escape the photoactivated region. Alternately, changes in the effective viscosity of the aqueous lumen in response to perturbed RTN4 expression could also modulate transport. Further empirical measurements and in silico modeling may help overcome these limits and distinguish the alternate possibilities.

In terms of the methodology of the CPAC assay, to measure the signal arrival time of luminal proteins at respective distances, we averaged the signal of paGFP^ER within small regions of interest (ROIs; 2- μm width) at various distances from a photoactivation site. This spatial averaging limits our ability to resolve the role of heterogeneous ER structures (such as tubes, junctions, and sheets) in modulating luminal transport. Notably, the effect of ER structural heterogeneity on transport rates has been explored in other work 37,46 and was found to have little effect on the spatiotemporal scaling of a spreading photoactivated signal.

Although our simulations confirmed that the presence of nearby sheet subdomains should not affect the CPAC measurements (Figure S9), improving the spatiotemporal resolution of the assay may provide additional insights into the motion of luminal solutes within these architectures.

It should be noted that, regardless of the mechanism by which RTN4 overexpression perturbs luminal transports, the reduction in spreading rates is expected to lower Ca²⁺ release rates. The dynamics of local Ca²⁺ release from the ER lumen may also be limited by additional factors not included in the current study, such as the density, clustering, and activation of the inositol 1,4,5-trisphosphate receptors as well as luminal Ca²⁺ load and the concentration of buffer proteins. In recent work, we used live-cell measurements to account for some of these effects and to demonstrate that transport through a well-connected ER lumen plays a significant role in setting the magnitude of local Ca²⁺ release.³⁷ The current results provide a comprehensive connection between the morphological role of RTN4, the rate of luminal transport, the local release of ER Ca²⁺, and the consequent physiological effect of neurite outgrowth inhibition.

STAR*METHODS

Detailed methods are provided in the online version of this paper and include the following:





- KEY RESOURCES TABLE
- RESOURCE AVAILABILITY
 - Lead contact
 - Materials availability
 - o Data and code availability
- EXPERIMENTAL MODEL AND STUDY PARTICIPANT DETAILS
 - o Cell culture, transfections, and expression constructs
 - O Human iPS cells culture and differentiation
- METHOD DETAILS
 - o Lentiviral preparations
 - Antibodies and reagents
 - o Immunofluorescence analysis
 - Microscopy Imaging and analyses
 - Simulations of transport in ER tubular networks
 - Neurite outgrowth analyses
 - Generation of RTN4 knockout cell lines by CRISPR
 - o Protein expression analyses
- QUANTIFICATION AND STATISTICAL ANALYSIS

SUPPLEMENTAL INFORMATION

Supplemental information can be found online at https://doi.org/10.1016/j.ceirep.2024.114357.

ACKNOWLEDGMENTS

We are extremely grateful to Luke D. Lavis (HHMI Janelia Research Campus, USA) for providing multiple HaloTag fluorescent ligands, including photoactivatable-Janelia Fluor 646 (paJ646), Joerg Bewersdorf (Yale University) for a plasmid, Gregory Strachan (Institute of Metabolic Science, University of Cambridge, UK) for invaluable technical support for setting up photoactivatable pulse-chase assays, the CIMR Flow Cytometry Core Facility (Cambridge Institute for Medical Research, UK) for cell sorting/flow cytometry analysis, and David Ron and Jonathon Nixon-Abell (Cambridge Institute for Medical Research. UK) for reagents and discussions. This work is supported by the UK Dementia Research Institute (award UK DRI-2004) through UK DRI Ltd., principally funded by the Medical Research Council (to E.A.). E.A. was further supported by Evelyn Trust and Alzheimer's Society grant AS-525 (AS-PhD-19a-015). E.F.K. and L.M.W. were supported by US National Science Foundation grants 2034482 and 2034486. Additional support for E.F.K. was provided by a Cottrell Scholar Award from the Research Corporation for Science Advancement and by the Hellman Fellows Fund. J.E.C. was supported by the MRC (Ref. MCMB MR/V028669/1).

AUTHOR CONTRIBUTIONS

Conceptualization, E.F.K. and E.A.; investigation, T.K., P.P., C.C.C., V.D., M.A.A., C.H., A.I.B., K.M.X., A.A., J.E.C., M.J.V.W., K.M.K., L.M.E., and S.S.; formal analysis, T.K., P.P., C.C.C., V.D., A.I.B., K.M.X., A.A., M.J.V.W., K.M.K., and S.S.; writing – original draft, T.K., E.F.K., and E.A.; writing – review & editing, T.K., J.E.C., L.M.W., E.F.K., and E.A.; resources, D.M.D.B., E.M., and L.M.W.; funding acquisition, J.E.C., L.M.W., E.F.K., and E.A.

DECLARATION OF INTERESTS

The authors declare no competing interests.

Received: February 14, 2024 Revised: March 1, 2024 Accepted: May 29, 2024 Published: July 1, 2024

REFERENCES

Voeltz, G.K., Prinz, W.A., Shibata, Y., Rist, J.M., and Rapoport, T.A. (2006).
 A class of membrane proteins shaping the tubular endoplasmic reticulum.
 Cell 124, 573–586. https://doi.org/10.1016/J.CELL.2005.11.047.

- Bastide, A., Peretti, D., Knight, J.R.P., Grosso, S., Spriggs, R.V., Pichon, X., Sbarrato, T., Roobol, A., Roobol, J., Vito, D., et al. (2017). RTN3 Is a Novel Cold-Induced Protein and Mediates Neuroprotective Effects of RBM3. Curr. Biol. 27, 638–650. https://doi.org/10.1016/J.CUB.2017. 01.047.
- Fu, H., Possenti, A., Freer, R., Nakano, Y., Hernandez Villegas, N.C., Tang, M., Cauhy, P.V.M., Lassus, B.A., Chen, S., Fowler, S.L., et al. (2019). A tau homeostasis signature is linked with the cellular and regional vulnerability of excitatory neurons to tau pathology. Nat. Neurosci. 22, 47–56. https:// doi.org/10.1038/S41593-018-0298-7.
- Murayama, K.S., Kametani, F., Saito, S., Kume, H., Akiyama, H., and Araki, W. (2006). Reticulons RTN3 and RTN4-B/C interact with BACE1 and inhibit its ability to produce amyloid beta-protein. Eur. J. Neurosci. 24, 1237– 1244. https://doi.org/10.1111/J.1460-9568.2006.05005.X.
- Sharoar, M.G., Shi, Q., Ge, Y., He, W., Hu, X., Perry, G., Zhu, X., and Yan, R. (2016). Dysfunctional tubular endoplasmic reticulum constitutes a pathological feature of Alzheimer's disease. Mol. Psychiatry 21, 1263–1271. https://doi.org/10.1038/MP.2015.181.
- Blackstone, C., O'Kane, C.J., and Reid, E. (2011). Hereditary spastic paraplegias: membrane traffic and the motor pathway. Nat. Rev. Neurosci. 12, 31–42. https://doi.org/10.1038/NRN2946.
- Blackstone, C. (2018). Converging cellular themes for the hereditary spastic paraplegias. Curr. Opin. Neurobiol. 51, 139–146. https://doi.org/10. 1016/J.CONB.2018.04.025.
- Montenegro, G., Rebelo, A.P., Connell, J., Allison, R., Babalini, C., D'Aloia, M., Montieri, P., Schüle, R., Ishiura, H., Price, J., et al. (2012). Mutations in the ER-shaping protein reticulon 2 cause the axon-degenerative disorder hereditary spastic paraplegia type 12. J. Clin. Invest. 122, 538–544. https://doi.org/10.1172/JCl60560.
- Zou, Y., He, W., Wang, K., Han, H., Xiao, T., Chen, X., Zhou, B., Tan, J., Xia, K., Tang, B., et al. (2018). Identification of rare RTN3 variants in Alzheimer's disease in Han Chinese. Hum. Genet. 137, 141–150. https://doi.org/10. 1007/S00439-018-1868-1.
- Powers, R.E., Wang, S., Liu, T.Y., and Rapoport, T.A. (2017). Reconstitution of the tubular endoplasmic reticulum network with purified components. Nature 543, 257–260. https://doi.org/10.1038/NATURE21387.
- Kim, J.E., Li, S., Grand Pré, T., Qiu, D., and Strittmatter, S.M. (2003). Axon regeneration in young adult mice lacking Nogo-A/B. Neuron 38, 187–199. https://doi.org/10.1016/S0896-6273(03)00147-8.
- Simonen, M., Pedersen, V., Weinmann, O., Schnell, L., Buss, A., Ledermann, B., Christ, F., Sansig, G., Van Der Putten, H., and Schwab, M.E. (2003). Systemic deletion of the myelin-associated outgrowth inhibitor Nogo-A improves regenerative and plastic responses after spinal cord injury. Neuron 38, 201–211. https://doi.org/10.1016/S0896-6273(03) 00226-5.
- Wu, H., and Voeltz, G.K. (2021). Reticulon-3 Promotes Endosome Maturation at ER Membrane Contact Sites. Dev. Cell 56, 52–66.e7. https://doi. org/10.1016/J.DEVCEL.2020.12.014.
- GrandPré, T., Nakamura, F., Vartanian, T., and Strittmatter, S.M. (2000).
 Identification of the Nogo inhibitor of axon regeneration as a Reticulon protein. Nature 403, 439–444. https://doi.org/10.1038/35000226.
- Kim, J.E., Bonilla, I.E., Qiu, D., and Strittmatter, S.M. (2003). Nogo-C is sufficient to delay nerve regeneration. Mol. Cell. Neurosci. 23, 451–459. https://doi.org/10.1016/S1044-7431(03)00076-9.
- Pernet, V., Joly, S., Dalkara, D., Schwarz, O., Christ, F., Schaffer, D., Flannery, J.G., and Schwab, M.E. (2012). Neuronal Nogo-A upregulation does not contribute to ER stress-associated apoptosis but participates in the regenerative response in the axotomized adult retina. Cell Death Differ. 19, 1096–1108. https://doi.org/10.1038/CDD.2011.191.
- Pot, C., Simonen, M., Weinmann, O., Schnell, L., Christ, F., Stoeckle, S., Berger, P., Rülicke, T., Suter, U., and Schwab, M.E. (2002). Nogo-A expressed in Schwann cells impairs axonal regeneration after peripheral

Article



- nerve injury. J. Cell Biol. *159*, 29–35. https://doi.org/10.1083/JCB. 200206068.
- Fournier, A.E., GrandPre, T., and Strittmatter, S.M. (2001). Identification of a receptor mediating Nogo-66 inhibition of axonal regeneration. Nature 409, 341–346. https://doi.org/10.1038/35053072.
- Farías, G.G., Fréal, A., Tortosa, E., Stucchi, R., Pan, X., Portegies, S., Will, L., Altelaar, M., and Hoogenraad, C.C. (2019). Feedback-Driven Mechanisms between Microtubules and the Endoplasmic Reticulum Instruct Neuronal Polarity. Neuron 102, 184–201.e8. https://doi.org/10.1016/J. NEURON.2019.01.030.
- Rämö, O., Kumar, D., Gucciardo, E., Joensuu, M., Saarekas, M., Vihinen, H., Belevich, I., Smolander, O.P., Qian, K., Auvinen, P., et al. (2016). NOGO-A/RTN4A and NOGO-B/RTN4B are simultaneously expressed in epithelial, fibroblast and neuronal cells and maintain ER morphology. Sci. Rep. 6, 35969. https://doi.org/10.1038/SREP35969.
- Schroeder, L.K., Barentine, A.E.S., Merta, H., Schweighofer, S., Zhang, Y., Baddeley, D., Bewersdorf, J., and Bahmanyar, S. (2019). Dynamic nanoscale morphology of the ER surveyed by STED microscopy. J. Cell Biol. 218, 83–96. https://doi.org/10.1083/JCB.201809107.
- Fernandopulle, M.S., Prestil, R., Grunseich, C., Wang, C., Gan, L., and Ward, M.E. (2018). Transcription Factor-Mediated Differentiation of Human iPSCs into Neurons. Curr. Protoc. Cell Biol. 79, e51. https://doi.org/ 10.1002/CPCB.51.
- Gao, G., Zhu, C., Liu, E., and Nabi, I.R. (2019). Reticulon and CLIMP-63 regulate nanodomain organization of peripheral ER tubules. PLoS Biol. 17, e3000355. https://doi.org/10.1371/JOURNAL.PBIO.3000355.
- Hu, J., Shibata, Y., Zhu, P.P., Voss, C., Rismanchi, N., Prinz, W.A., Rapoport, T.A., and Blackstone, C. (2009). A class of dynamin-like GTPases involved in the generation of the tubular ER network. Cell 138, 549–561. https://doi.org/10.1016/J.CELL.2009.05.025.
- Zhang, X., Ding, X., Marshall, R.S., Paez-Valencia, J., Lacey, P., Vierstra, R.D., and Otegui, M.S. (2020). Reticulon proteins modulate autophagy of the endoplasmic reticulum in maize endosperm. Elife 9, e51918. https:// doi.org/10.7554/ELIFE.51918.
- Grumati, P., Morozzi, G., Hölper, S., Mari, M., Harwardt, M.L.I.E., Yan, R., Müller, S., Reggiori, F., Heilemann, M., and Dikic, I. (2017). Full length RTN3 regulates turnover of tubular endoplasmic reticulum via selective autophagy. Elife 6, e25555. https://doi.org/10.7554/ELIFE.25555.
- Shibata, Y., Voeltz, G.K., and Rapoport, T.A. (2006). Rough sheets and smooth tubules. Cell *126*, 435–439. https://doi.org/10.1016/J.CELL. 2006.07.019.
- Nixon-Abell, J., Obara, C.J., Weigel, A.V., Li, D., Legant, W.R., Xu, C.S., Pasolli, H.A., Harvey, K., Hess, H.F., Betzig, E., et al. (2016). Increased spatiotemporal resolution reveals highly dynamic dense tubular matrices in the peripheral ER. Science 354, aaf3928. https://doi.org/10.1126/SCI-ENCE.AAF3928.
- Hoffman, D.P., Shtengel, G., Xu, C.S., Campbell, K.R., Freeman, M., Wang, L., Milkie, D.E., Pasolli, H.A., Iyer, N., Bogovic, J.A., et al. (2020). Correlative three-dimensional super-resolution and block-face electron microscopy of whole vitreously frozen cells. Science 367, eaaz5357. https://doi.org/10.1126/SCIENCE.AAZ5357.
- Jozsef, L., Tashiro, K., Kuo, A., Park, E.J., Skoura, A., Albinsson, S., Rivera-Molina, F., Harrison, K.D., Iwakiri, Y., Toomre, D., and Sessa, W.C. (2014). Reticulon 4 is necessary for endoplasmic reticulum tubulation, STIM1-Orai1 coupling, and store-operated calcium entry. J. Biol. Chem. 289, 9380–9395. https://doi.org/10.1074/JBC.M114.548602.
- Holcman, D., Parutto, P., Chambers, J.E., Fantham, M., Young, L.J., Marciniak, S.J., Kaminski, C.F., Ron, D., and Avezov, E. (2018). Single particle trajectories reveal active endoplasmic reticulum luminal flow. Nat. Cell Biol. 20, 1118–1125. https://doi.org/10.1038/S41556-018-0192-2.
- Happel, J., and Brenner, H. (1983). Low Reynolds number hydrodynamics, with special applications to particulate media. Mech. Fluids Transp. Process. 1, 1–22.

- Patterson, G.H., and Lippincott-Schwartz, J. (2002). A photoactivatable GFP for selective photolabeling of proteins and cells. Science 297, 1873–1877. https://doi.org/10.1126/SCIENCE.1074952.
- Sun, Y., Yu, Z., Obara, C.J., Mittal, K., Lippincott-Schwartz, J., and Koslover, E.F. (2022). Unraveling trajectories of diffusive particles on networks. Phys. Rev. Res. 4, 023182. https://doi.org/10.1103/PHYSREVRE-SEARCH.4.023182/FIGURES/6/MEDIUM.
- Akiyama, H., Matsu-Ura, T., Mikoshiba, K., and Kamiguchi, H. (2009). Control of neuronal growth cone navigation by asymmetric inositol 1,4,5-tri-sphosphate signals. Sci. Signal. 2, ra34. https://doi.org/10.1126/SCISIGNAL.2000196.
- Wada, F., Nakata, A., Tatsu, Y., Ooashi, N., Fukuda, T., Nabetani, T., and Kamiguchi, H. (2016). Myosin Va and Endoplasmic Reticulum Calcium Channel Complex Regulates Membrane Export during Axon Guidance. Cell Rep. 15, 1329–1344. https://doi.org/10.1016/J.CELREP.2016. 04.021
- Crapart, C.C., Scott, Z.C., Konno, T., Sharma, A., Parutto, P., Bailey, D.M.D., Westrate, L.M., Avezov, E., and Koslover, E.F. (2024). Luminal transport through intact endoplasmic reticulum limits the magnitude of localized Ca2+ signals. Proc. Natl. Acad. Sci. USA 121, e2312172121. https://doi.org/10.1073/PNAS.2312172121.
- Berridge, M.J., and Irvine, R.F. (1984). Inositol trisphosphate, a novel second messenger in cellular signal transduction. Nature 312, 315–321. https://doi.org/10.1038/312315A0.
- Ross, C.A., Meldolesi, J., Milner, T.A., Satoh, T., Supattapone, S., and Snyder, S.H. (1989). Inositol 1,4,5-trisphosphate receptor localized to endoplasmic reticulum in cerebellar Purkinje neurons. Nature 339, 468–470. https://doi.org/10.1038/339468A0.
- Avezov, E., Konno, T., Zyryanova, A., Chen, W., Laine, R., Crespillo-Casado, A., Melo, E.P., Ushioda, R., Nagata, K., Kaminski, C.F., et al. (2015). Retarded PDI diffusion and a reductive shift in poise of the calcium depleted endoplasmic reticulum. BMC Biol. 13, 2. https://doi.org/10.1186/S12915-014-0112-2.
- Greotti, E., Wong, A., Pozzan, T., Pendin, D., and Pizzo, P. (2016). Characterization of the ER-Targeted Low Affinity Ca(2+) Probe D4ER. Sensors 16, 1419. https://doi.org/10.3390/S16091419.
- Seiler, S., Di Santo, S., and Widmer, H.R. (2016). Nogo-A Neutralization Improves Graft Function in a Rat Model of Parkinson's Disease. Front. Cell. Neurosci. 10, 87. https://doi.org/10.3389/FNCEL.2016.00087.
- Meininger, V., Genge, A., van den Berg, L.H., Robberecht, W., Ludolph, A., Chio, A., Kim, S.H., Leigh, P.N., Kiernan, M.C., Shefner, J.M., et al. (2017). Safety and efficacy of ozanezumab in patients with amyotrophic lateral sclerosis: a randomised, double-blind, placebo-controlled, phase 2 trial. Lancet Neurol. 16, 208–216. https://doi.org/10.1016/S1474-4422(16) 30399-4.
- Zurek, N., Sparks, L., and Voeltz, G. (2011). Reticulon short hairpin transmembrane domains are used to shape ER tubules. Traffic 12, 28–41. https://doi.org/10.1111/J.1600-0854.2010.01134.X.
- Htet, P.H., Avezov, E., and Lauga, E. (2024). Fluid mechanics of luminal transport in actively contracting endoplasmic reticulum. Elife 13, 1–39. https://doi.org/10.7554/ELIFE.93518.1.
- Scott, Z.C., Koning, K., Vanderwerp, M., Cohen, L., Westrate, L.M., and Koslover, E.F. (2023). Endoplasmic reticulum network heterogeneity guides diffusive transport and kinetics. Biophys. J. 122, 3191–3205. https://doi.org/10.1016/J.BPJ.2023.06.022.
- Bottanelli, F., Kromann, E.B., Allgeyer, E.S., Erdmann, R.S., Wood Baguley, S., Sirinakis, G., Schepartz, A., Baddeley, D., Toomre, D.K., Rothman, J.E., and Bewersdorf, J. (2016). Two-colour live-cell nanoscale imaging of intracellular targets. Nat. Commun. 7, 10778. https://doi.org/10.1038/NCOMMS10778.
- Dora, M., and Holcman, D. (2020). Active flow network generates molecular transport by packets: case of the endoplasmic reticulum. Proc. Biol. Sci. 287, 20200493. https://doi.org/10.1098/RSPB.2020.0493.





- Matthews, E.A., and Dietrich, D. (2015). Buffer mobility and the regulation of neuronal calcium domains. Front. Cell. Neurosci. 9, 48. https://doi.org/ 10.3389/FNCEL.2015.00048.
- Nash, P.D., Opas, M., and Michalak, M. (1994). Calreticulin: not just another calcium-binding protein. Mol. Cell. Biochem. 135, 71–78. https://doi.org/10.1007/BF00925962.
- Berg, S., Kutra, D., Kroeger, T., Straehle, C.N., Kausler, B.X., Haubold, C., Schiegg, M., Ales, J., Beier, T., Rudy, M., et al. (2019). ilastik: interactive machine learning for (bio)image analysis. Nat. Methods 16, 1226–1232. https://doi.org/10.1038/S41592-019-0582-9.
- Sun, X.P., Callamaras, N., Marchant, J.S., and Parker, I. (1998). A continuum of InsP3-mediated elementary Ca2+ signalling events in Xenopus oocytes. J. Physiol. 509, 67–80. https://doi.org/10.1111/J.1469-7793.1998.067BO.X.
- Radding, W., Jordan, S.E., Hester, R.B., and Blair, H.C. (1999). Intracellular calcium puffs in osteoclasts. Exp. Cell Res. 253, 689–696. https://doi.org/10.1006/EXCR.1999.4714.
- Yang, Z., and Koslover, E.F. (2023). Diffusive exit rates through pores in membrane-enclosed structures. Phys. Biol. 20:026001. https://doi.org/ 10.1088/1478-3975/ACB1EA.



STAR***METHODS**

KEY RESOURCES TABLE

REAGENT or RESOURCE	SOURCE	IDENTIFIER
Antibodies		
Anti-Nogo A + B	Abcam	Cat# ab47085; RRID: AB_881718
Anti-MAP2	Abcam	Cat# ab5392; RRID: AB_2138153
Anti-Synaptophysin1	Synaptic Systems	Cat# 101 004; RRID: AB_1210382
Anti-beta Tubulin	Thermo Fisher Scientific	Cat# MA5-16308; RRID: AB_2537819
Goat anti-Rabbit IgG (H + L) Highly Cross-Adsorbed Secondary Antibody, Alexa Fluor [™] 488	Thermo Fisher Scientific	Cat# A11034; RRID: AB_2576217
Goat anti-Mouse IgG2a Cross-Adsorbed Secondary Antibody, Alexa Fluor TM 555	Thermo Fisher Scientific	Cat# A-21137; RRID: AB_2535776
Goat anti-Chicken IgY (H + L) Secondary Antibody, Alexa Fluor TM 568	Thermo Fisher Scientific	Cat# A-11041; RRID: AB_2534098
Goat anti-Guinea Pig IgG (H + L) Highly Cross-Adsorbed Secondary Antibody, Alexa Fluor TM 488	Thermo Fisher Scientific	Cat# A-11073; RRID: AB_2534117
Bacterial and virus strains		
NEB® 5-alpha Competent E. coli	New England Biolabs	C2987I
ncucyte® Neuroburst Orange Lentivirus	Sartorius	4736
Chemicals, peptides, and recombinant proteins		
HaloTag® TMR Ligand	Promega	G8251
laloTag® diAcFAM Ligand	Promega	G8272
anelia Fluor® 646 HaloTag® Ligand	Promega	GA1120
SNAP-Cell® 505-Star	New England Biolabs	S9103S
SNAP-Cell® 647-SiR	New England Biolabs	S9102S
⁻ hapsigargin	Cayman Chemical	CAY10522-1 mg
si-IP3/PM	Bio-Techne	6210
Critical commercial assays		
PureYield TM Plasmid Maxiprep System	Promega	A2393
Vizard® SV Gel and PCR Clean-Up System	Promega	A9282
NEBuilder® HiFi DNA Assembly Master Mix	New England Biolabs	E2621L
Experimental models: Cell lines		
COS-7	ATCC	RRID: CVCL_0224
HEK293T	ATCC	RRID: CVCL_0063
SH-SY5Y	ATCC	RRID: CVCL_0019
Human: NGN2 iPSCs	M. Ward (National Institutes of Health) ²²	RRID: CVCL_C7XJ
RTN4 KO COS-7	This study	N/A
RTN4 KO SH-SY5Y	This study	N/A
RTN4 KO NGN2 iPSCs	This study	N/A
Digonucleotides		
Rtn4_sgRNA_top: 5'-CACCGCAGATGAAGGCCACCCATTC-3'	This study	N/A
Rtn4_sgRNA_bottom: 5'-AAACGAATGGGTGGCCTTCATCTGC-3'	This study	N/A
Hu_Rtn4_genotying_r: 5'-GGTATAGCTCAAGCAAATAACTGC-3'	This study	N/A

(Continued on next page)



Continued		
REAGENT or RESOURCE	SOURCE	IDENTIFIER
Hu_Rtn4_genotying_f 5'-AGTATTCAGCATTGTGAGCGTA-3'	This study	N/A
COS7 Rtn4 KO_genotyping-f 5'-GAGTGGGTTTAAAATGTGGG-3'	This study	N/A
COS7 Rtn4 KO_genotyping-r 5'-GTATATCCTAAAGCTGATGGTCAC-3'	This study	N/A
Recombinant DNA		
pSpCas9(BB)-2A-GFP	Addgene	RRID: Addgene_48138
pSpCas9(BB)-2A-GFP_gRNA RTN4	This study	N/A
pLV_Exp_Puro-TRE3G_Xbal_Hu Rtn3A-TEV- HaloTag	This study	N/A
pcDNA3-ER-GCaMP3	Addgene	RRID: Addgene_64854
pFLAG_ER mCherry	gift from D.Ron ⁴⁰	N/A
Halo-Sec61β	gift from J. Bewersdorf ⁴⁷	N/A
pmPA-GFP-ER-5	Addgene	RRID: Addgene_57132
pMD1g/pRRE	Addgene	RRID: Addgene_12251
pRSV-Rev	Addgene	RRID: Addgene_12253
pDM2.G	Addgene	RRID: Addgene_12259
mCherry_SBP_RTN4A	gift from G.G.Farías ¹⁹	N/A
ER-Crowding_FRET1_CRH2_KDEL_pCDNA3-1(+)	gift from D. Ron ³¹	N/A
pLV_Rtn4-SNAP	This study	N/A
pLV_TRE3G_hRTN4a-Halo	This study	N/A
D4ER	gift from D. Ron ⁴¹	N/A
SNAP-Sec61β	This study	N/A
mEmerald-Calnexin	Addgene	RRID: Addgene_54021
mcherry_RTN4a	L.M.Westrate ⁴⁴	N/A
pCMV_mCherry_SBP	This study	N/A
RTN2C-mEmerald-N1	This study	N/A
pLV_RTN4c-SNAP	This study	N/A
pCMV_mCherry-SBP-RTN2C	This study	N/A
pCMV_mCherry-SBP-Sec61b	This study	N/A
Software and algorithms		
Prism9	Graph Pad	https://www.graphpad.com/; RRID: SCR_002798
Fiji (ImageJ)	NIH, USA	https://fiji.sc/; RRID: SCR_002285
Leica Application Suite X	Leica	https://www.leica-microsystems.com/ products/microscope-software/p/ leica-las-x-ls/; RRID: SCR_013673
MATLAB	MathWorks	http://www.mathworks.com/products/ matlab/; RRID: SCR_001622
IncuCyte S3 Live Cell Analysis System	Sartorius	https://www.sartorius.com/en/ products/live-cell-imaging-analysis/ live-cell-analysis-instruments/s3-live- cell-analysis-instrument#id-797316; RRID: SCR_023147
Other		
The custom code for analysing CPAC measurements	This study	https://doi.org/10.5281/zenodo.11206308
The custom code for the finite volume simulation of concentration profiles spreading over network structures	This study	https://doi.org/10.5281/zenodo.11206293

Article



RESOURCE AVAILABILITY

Lead contact

Further information and requests for resources and reagents should be directed to and will be fulfilled by the lead contact, Edward Avezov (ea347@cam.ac.uk).

Materials availability

All materials generated in this study will be shared upon request.

Data and code availability

- Data reported in this work will be made available from the lead contact upon request.
- The custom code for analysing CPAC measurements and the finite volume simulation of concentration profiles spreading over network structures are available on https://doi.org/10.5281/zenodo.11206308 and https://doi.org/10.5281/zenodo.11206293, respectively.
- Any additional information required to reanalyse the data reported in this work is available from the lead contact upon request.

EXPERIMENTAL MODEL AND STUDY PARTICIPANT DETAILS

Cell culture, transfections, and expression constructs

COS-7 (RRID: CVCL_0224) and HEK293T (RRID: CVCL_0063) cells were cultured in Dulbecco's modified Eagle's medium (DMEM) supplemented with 10% fetal bovine serum (FBS), 2 mM L-Glutamine and 100 U/mL Penicillin-Streptomycin (P/S). SH-SY5Y (RRID: CVCL_0019) cells were cultured in DMEM/F12 (1:1) medium supplemented with 10% FBS, 2 mM L-Glutamine, 100 U/mL P/S and 1 × non-essential amino acids (NEAA, 11140035, Gibco). Transfections were performed using the Neon Transfection System (Invitrogen). Descriptions of the plasmids used in this study were presented in the STAR Methods section.

Human iPS cells culture and differentiation

Human iPSCs with Neurogenin-2 (NGN2) transgene stably integrated into a 'safe-harbour' locus under a doxycycline (Dox)-inducible promoter were cultured in TeSR-E8 medium (05990, STEMCELL Technologies). Differentiation into cortical neurons (iNeurons) was performed according to previously described protocols with slight modifications. ²² Briefly, at day 1 and day 2 of differentiation, iPSCs were cultured in DMEM/F12 medium supplemented with 1 x *N*-2 supplement, 2 mM L-Glutamine, 1 x NEAA, 50 nM 2-Mercaptoethanol (2ME), 100 U/mL P/S, and 1 μg/mL Dox and changed daily. After day 3, culture medium was replaced to Neurobasal medium (Thermo Fisher) supplemented with 1 x B-27 supplement, 2 mM L-Glutamine, 50 nM 2ME, 100 U/mL P/S, and 1 μg/mL Dox, 10 ng/mL NT-3, and 10 ng/mL Brain-derived neurotrophic factor (BDNF). Full-media changes made up until day 6, after which, half-media changes were made every other day until day 21.

Neurophysiological activity of differentiated iNeurons was assessed using Neuroburst Orange, a neuron-expressible genetically encoded calcium indicator (#4736, Sartorius). Lentiviral particles of Neuroburst were delivered into iNeurons (day 18), and Ca²⁺ fluctuations were recorded and analysesd using the Incucyte S3 (Sartorius) (Video S1).

METHOD DETAILS

Lentiviral preparations

Lentiviral particle was produced by transfecting HEK293T cells with the RTN4a-Halo expression vector and three helper plasmids (3^{rd} generation packaging system) expressing Gag, Pol, Rev, and VSVG. The transfection was carried out using the Polyethylenimine (PEI, Polysciences, 23966–1) with a plasmid ratio of 1:1:1:1. The lentivirus-containing medium was harvested 48 and 72 h after transfection and pre-cleaned with a 3,500 g centrifugation and a 0.45 μ m filtration. The lentivirus-containing medium was subsequently collected by an ultracentrifugation (100,000 g for 2 h). After a removal of the supernatant, the pellet of lentiviral particle was re-suspended in PBS.

Antibodies and reagents

Rabbit polyclonal antibodies to RTN4 (ab47085) and chicken polyclonal antibodies to microtubule-associated protein 2 (MAP2, ab5392) were obtained from Abcam. Guinea Pig polyclonal antibodies to synaptophysin 1 (101 004) was obtained from Synaptic Systems (Göttingen, Germany). Mouse monoclonal antibodies to β-tubulin (MA5-16308), Alexa Fluor 488-conjugated goat anti-rabbit secondary antibodies (A-11034), Alexa Fluor 555-conjugated goat anti-mouse secondary antibodies (A-21137), Alexa Fluor 568-conjugated goat anti-chicken secondary antibodies (A-11041), and Alexa Fluor 488-conjugated goat anti-guinea pig secondary antibodies (A-11073) were obtained from Thermo Fisher Scientific. Caged-IP₃ (ci-IP₃/PM, #6210) was obtained from Bio-Techne. HaloTag TMR (G8251), HaloTag diAcFAM (G8272), and Janelia Fluor 646-conjugated HaloTag ligand (J646, not photoactivatable, GA1120) were obtained from Promega (Madison, WI, USA). HaloTag-ligand conjugated photoactivatable-Janelia Fluor 646 (paJ646) was a gift from Dr. Luke D. Lavis (HHMI Janelia Research Campus, USA). SNAP-Cell 505-Star (S9103S) and SNAP-Cell





647-SiR (NEB S9102S) were obtained from New England Biolabs (NEB, Ipswich, MA, USA). Thapsigargin (10522-1mg-CAY) was obtained from Cambridge Bioscience (Cambridge, UK).

Immunofluorescence analysis

Prior to immunofluorescence staining, cells were fixed with 2% PFA, 2% glutaraldehyde, 100 mM cacodylate (pH 7.4), and 2 mM CaCl₂ for 30 min at room temperature (RT), permeabilised with 0.5% Triton X-100/PBS for 30 min at RT, and blocked with 10% goat serum/PBS for 30 min at RT. Primary antibodies were used with 1:1000 dilution overnight at 4°C, and secondary antibodies were used with 1:1000 dilution for 1 h at RT. Images were acquired with a confocal microscope (STELLARIS8, Leica, Wetzlar, Germany) with lightning deconvolution.

Microscopy – Imaging and analyses Lattice-SIM

Lattice-SIM imaging was performed using a Zeiss Elyra7 microscope using a 63×1.4 NA oil immersion objective. Endogenous RTN4 label with antibody and transfected mCherry^{ER} were excited at 488 nm and 561 nm respectively and images were captured simultaneously with 40 ms exposure time using an Optosplit beam splitter and two pco.edge sCMOS cameras. Cells were imaged in-live, and Z-stacks were acquired with 55 nm sectioning. Images were processed using Zeiss' SIM2 algorithm, in 3 dimensions using the "standard – live" settings with the sectioning set at 92 and intensity scaled with the original image. A linear background subtraction was performed on both channels of the processed image and pixel number was increased 4-fold.

Transmission electron microscopy (TEM)

COS-7 cells expressing Halo-Sec61βTMR (Figure S6), mCherry (WT and RTN4 KO in Figure 2E), and mCherry-RTN4a (RTN4a OE in Figure 2E) were sorted by flow cytometry (FACS Melody, BD Biosciences, San Jose, CA) and seeded on coverslips 24 h post transfection. Following further 24 h culture, cells were fixed in 2.5% glutaraldehyde, 2% paraformaldehyde for 1 h at RT and then overnight in the fresh fixative at 4°C. The samples were then washed with dH₂O and treated with 1% osmium tetroxide, 1.5% potassium ferricyanide for 1 h at RT. Subsequently, cells were washed again and gradually dehydrated in ethanol (70%, 90%, 100%), infiltrated with Epon resin and baked for 48 h at 60°C. Blocks were sectioned at 60 nm onto 200 mesh CU grids using an EM UC7 ultramicrotome (Leica, Wetzlar, Germany). Grids were post-stained with 1% uranyl acetate and lead citrate, and images were acquired using a transmission electron microscope HT7800 (Hitachi, Tokyo, Japan) at 100 kV. Following calibration, ER tubule radius was measured using ImageJ software (National Institute of Health, Bethesda, MD, USA).

Quantifying tube width from relative fluorescence analysis

To calculate the average radius of ER tubules, we leveraged the integrated fluorescence intensities from labeled ER membrane proteins (mEmerald-Calnexin in Figure 2C and Halo-Sec61β in Figure 2D).

Images of mEmerald-Calnexin were obtained as follows. COS-7 cells were grown at 37° C with 5% CO₂ in DMEM medium (Gibco) containing 10% fetal bovine serum and 1% penicillin/streptomycin (Invitrogen). Emerald-Calnexin was a gift from Michael Davidson (Addgene plasmid #54021) and mCherry-RTN4a was previously described. He plasmid transfections were performed with the following amounts of DNA per mL: $0.2 \, \mu g$ mEmerald-Calnexin with either $0.2/0.4 \, \mu g$ mCherry-RTN4a or $0.2/0.4 \, \mu g$ mCherry empty as a control (see figure for respective concentration and transfection setup). 24 h post transfection, cells were fixed at room temperature with 4% paraformaldehyde plus 0.5% glutaraldehyde in PBS. All images were acquired on an inverted fluorescence microscope (Nikon A1 confocal microscope) equipped with a $100x \, NA \, 1.45$ oil objective.

For measurements of RTN4 KO and the corresponding WT control cells, Halo-Sec61 β was transfected as an ER membrane marker using the Neon transfection system (Thermo Fisher Scientific). 24 h post-transfection, cells were stained with a HaloTag-ligand, di-AcFAM (200 nM, 1 h) and were subjected to live imaging using a STELLARIS8 laser scanning system with a 63× oil objective (An HC PL APO CS2 63x/1.40 OIL).

For image analysis purposes, we assumed that the labeled protein concentrations per membrane surface area are constant throughout a few-micron wide region within a given image, and that the integrated fluorescence intensity in any cellular subregion is therefore proportional to the total ER membrane surface area in that subregion. For a region containing a single tubule of radius R and length L, the total fluorescence intensity is taken as $I_{\text{tube}} = a(2\pi R L)$, where a is a pre-factor incorporating protein density and fluorescent intensity per protein. For a peripheral sheet region, assumed to correspond to a single flat ER structure, surrounded by two membranes of area A, the integrated fluorescence intensity is taken as $I_{\text{sheet}} = a(2A)$. By comparing intensities in a peripheral sheet and nearby tubule regions, the tubule radius can be approximated from the ratio of the two, according to the relationship in Equation 1. Because the calculation normalises by the area and length of the selected segments of sheets and tubules, the values of A and L need not correspond to a complete sheet or entire tubule. Moreover, by comparing nearby sheets and tubules, we negate the effect of any cell-scale variations in fluorescence intensity. We averaged potential spatial variation in tubular width by pooling data from all cellular regions with a well-defined tubular network.

Each estimate of local tubule radius is based on a manually selected sheet segment and several nearby local tube segments. The mean \pm SD area of selected sheet segments was $0.88 \pm 1.2 \,\mu\text{m}^2$ and the mean \pm SD of nearby selected tube segment length was $4.8 \pm 2.9 \,\mu\text{m}$. There was no significant difference in either the selected sheet area of the tube length between each condition and its respective control (p > 0.1 via a two-sample Kolmogorov-Smirnov test), with the exception that sheet areas in RTN4 OE cells were slightly smaller than the control (p = 0.043) due to there being fewer extensive peripheral sheets to be found in this condition. Notably,



reducing all control sheet segment areas by \sim 40% via erosion had no significant effect on the estimates of tubule radius (ρ = 0.85 compared to original measurements). Similarly reducing the tube segment lengths analyzed by 50% also had no significant effect (ρ = 0.47, compared to original measurements). We thus emphasize that, due to normalization of the calculation, the specific sizes of selected sheet and tube segments do not affect the results.

To process each individual image, background intensity is determined by selecting a region outside of the ER network and taking the median intensity in that region. The background signal is subtracted from the image prior to analysis. We then manually identify a peripheral sheet region with well-defined nearby tubules (e.g., Figure 2C). We selected peripheral sheets, rather than those near the nucleus, to avoid challenges associated with stacked sheet structures. To avoid edge effects, the sheet ROI is eroded by a disc structuring element of radius 0.2 μ m. Nearby tubule regions are selected such that no tubule intersections or nearby encroaching tube or sheet regions appear alongside each individual tube segment. To incorporate fluorescence from the diffraction-limited area around each tube segment, the backbone of each segment is dilated by 0.2 μ m, yielding the pink regions in Figure 2C. The length of each tube region and area of the peripheral sheet region are then computed and incorporated into the analysis alongside the integrated fluorescence intensity in each tubule and sheet region. Multiple combinations of a peripheral sheet region and nearby tubules were selected in each individual image when possible and treated as distinct measurements of the local tubule radius.

Although the range of measurements for the tubule radius varied widely, the average over many structures in dozens of control wildtype cells (R = 51 \pm 12 nm, mean \pm SD, n = 141 independent regions) matched well to more detailed measurements reported with super-resolution imaging of tubular ER in COS-7 cells (R = 48 \pm 9 nm²³). Very similar tubule radii were measured in wildtype SH-SY5Y cells (R = 51 \pm 9 nm, n = 30). It should be noted that the current indirect approach has some advantages over the less accessible and more effort-intensive approaches. Namely, it can be carried out using standard confocal microscopy on live cells, thereby avoiding any potential artifacts associated with cell fixation.

A two-sample Kolmogorov-Smirnov test, designed for comparing data samples with no assumptions of Gaussian distribution, indicated that the distribution of tubule radii in cells with RTN4a overexpression or RTN4 knockout was significantly different from the distribution in control cells (p = 0.01 for COS-7 cells, p = 0.0003 for SH-SY5Y cells). Separate controls were carried out for each imaging run. Notably, when applied to comparing datasets from wildtype controls from different imaging runs, the same statistical test gave non-significant p-values, giving no reason to reject the hypothesis that the two samples were drawn from the same distribution of tubule radii. Namely, a comparison of WT COS-7 cells with labeled calnexin vs. Sec61 β membrane protein yielded p = 0.7, and a comparison of WT COS-7 cells and WT SH-SY5Y cells (using fluorescently labeled Sec61 β in both) yielded p = 0.5. These results imply that the measurements of tubule radii described here are relatively robust to the choice of visualised membrane protein, for the two cell types considered.

Assessment of alternate peripheral sheet morphologies effects (Figure S7): Recent super-resolution imaging studies have indicated that structures which appear as ER peripheral sheets in diffraction-limited confocal images may actually be composed of dense matrices of tubules²⁸ or may be studied with dynamic nano-scale holes.²¹ We consider briefly the potential effect of such alternate sheet morphologies on our estimates of the ER tubule radii via relative fluorescence analysis. The value of A in Equation 1 is in fact an apparent projected area for the putative sheet structure. Thus, the relationship between the estimated tube radius R_{est} and the true radius R_{true} can be expressed as $R_{\text{est}} = R_{\text{true}}$ (2 A/A_{true}) where A_{true} is the true membrane surface area within the sheet region.

From the measurements in the previous report,²¹ we assume the apparent sheets have a thickness of $h_s = 50$ nm and are perforated with holes of diameter $2r_h = 130$ nm. The density of holes is taken to be roughly $\rho = 10 \,\mu\text{m}^{-2}$. For simplicity, we assume the holes to be evenly spaced in a hexagonal lattice and assume that the membrane inside each hole can be treated as the inner half of a toroid (Figure S7A). The ratio of the true versus apparent area of such a perforated sheet structure can be computed as

$$\frac{A_{\text{true}}}{2A} = 1 - \frac{2\pi r_h^2}{\sqrt{3d^2}} + \frac{\pi^2 h_s}{3d^2} \left(r_h + \frac{h_s}{2} - \frac{h_s}{\pi} \right) \approx 1.05$$

where $d^2 = 2/(\sqrt{3}\rho)$ is the squared separation between holes. The resulting estimate is then $R_{est} = 0.95~R_{true}$, so that our estimated radius would be underestimating the true radius by only about 5%. We note that this error scales approximately linearly with the density of holes.

We next consider the possibility that the apparent sheets are actually dense matrices of tubules. For concreteness, assume that the tubules in the matrices have the same radius r_t as other peripheral tubes, and that they are arranged in a hexagonal lattice (Figure S7B). Using the estimates in the previous report, ²⁸ we take the gap size between parallel tubes to have extent $2r_h = 300$ nm in WT cells. We also assume that narrowing of the tubules with RTN4 overexpression will widen these gaps, so we can set $r_h = 200$ - r_t . The surface area A_j of each junction region is estimated as half the inner section of a toroid plus two flat sheets. The straight tubule sections have radius r_t and length $L = 2(r_h - r_t)/\sqrt{3}$. The overall ratio of true to apparent surface area for this structure is then given by.

The estimated tubule radius for each value of the true tubule radius is plotted in Figure S7C. We note that the model with dense tubule matrices (red curve) consistently predicts a high estimated radius (above 70 nm) and is thus largely inconsistent with our experimental measurements.





Continuous photoactivation chase (CPAC)

The assay was performed using a confocal microscope (SP8, Leica, Wetzlar, Germany) with a controlled environment (37° C, 5% CO₂). Images were acquired using a frame size of 512 × 512 pixels in the green (488 nm excitation, 495–545 nm emission), the red (555 nm excitation, 571–618 nm emission for TMR, or 567 nm excitation, 608–635 nm emission for mCherry), and the far-red (637 nm excitation, 645–700 nm emission) channels. After an acquisition of pre-photoactivation images, photoactivation illumination (405 nm, 100% laser power for both HaloTag-paJ646 and paGFP^{ER}) was introduced in a region of interest (photoactivation spot) for a duration of 300 (COS-7) or 150 (SH-SY5Y) frames (140 ms/frame), using the Fly mode (enabling image recording during the photoconverting illumination) in the FRAP wizard. Intensity of the photoactivation channel at the photoactivation spot as well as other regions of interest were plotted as a function of time during photoactivation, and fitted to a double-exponential function, to extract the half-time to reach plateau ($t_{1/2}$), that was used as an estimator of HaloTag-fused proteins or paGFP^{ER} mobility.

Photoconversion image analysis

The spread of proteins from the photoactivation site was quantified using custom code for image analysis and median rise-time estimation written in MATLAB (version 9.5.0, R2018b, Natick, Massachusetts: The MathWorks Inc.). The cell and nucleus shape were manually segmented from images of ER luminal marker (mCherry ER). The segmented area, consisting of the region inside the cell boundary but outside the nucleus, was eroded by 1 μ m to avoid edge effects.

The photoactivation region was directly segmented from the channel focused on the activation spot during the photoactivation phase. The centroid of the photoactivation region was set as the photoactivation center. The photoactivation region, with a 1μ m buffer, was removed from the cell area to be analyzed.

The segmented cell area was first divided into concentric ring regions of width 2 μ m, with the inner radius starting at 1 μ m intervals in distance from the photoactivation center. Each ring was then divided into wedge-shaped ROIs of arc-length 2 μ m, shifted by 1 μ m around the circle. Each wedge ROI was intersected with the segmented cell area, and only those ROIs with at least 2 μ m² of valid area (1 μ m² in SH-SY5Y cells) were retained for analysis.

Each of these ROIs yielded a fluorescence intensity time trace normalised by the ROI area (Figure S10A).

For each cell, the intensity time series after the start of photoactivation was fitted to a double-exponential function rising from the pre-photoactivation value to a maximum value set by the max value of the smoothed fluorescence signal in the photoactivated region. This fitting reflects the assumption that at infinite time, the fluorescence in the whole cell will equilibrate to that of the photoactivated region, even though the imaged timescales are generally too short to see this saturation for ROIs far from the photoactivated center.

The double-exponential fits were used to compute a half-time for the signal rise. Curves with insufficient signal-to-noise ratio (signal range less than twice the pre-photoactivation standard deviation) were removed from the analysis, as were those giving a half-time more than 5 times the recorded time span ($t_{1/2} > 350$ s seconds). The median half-time is computed for all remaining wedge regions at a given radius from the photoactivation center, from all cells in each dataset. Error bars were obtained by bootstrapping individual cells from each dataset and repeating the analysis. The error bars (standard deviation of the median) therefore give an indication of the cell-to-cell variation in each reported half-time.

When analysing the data specifically for RTN4 OE and RTN4 KO COS-7 cells, and their corresponding wild-type controls (Figure 4E), the curves of intensity rise at various distances from the point of photoactivation were fitted to a single-exponential function to estimate the arrival half-time to each region. This alternate approach was needed as it was found that the signal in many wedge regions near the photoactivation site substantially exceeded the signal in the photoactivation region itself, possibly due to increased bleaching in the photoactivated region, thus precluding a double exponential fit with a fixed maximum plateau. With a single-exponential, the curves could be fitted reasonably well, without the need to impose a predefined maximum value. All the curves in Figure 4E were analyzed with the same method, enabling meaningful comparison between the control measurements and the results of perturbed RTN4 expression.

The code for analysing CPAC measurements is available on https://doi.org/10.5281/zenodo.11206308.

Photo-uncaging of caged-IP₃ and imaging the ER Ca²⁺ release measurements

Prior to microscope imaging, cells were transfected to express GCaMP3^{ER}, an ER membrane-tethered Ca²⁺ sensor facing cytosolic side, and treated with caged-IP₃ (3 μ M, 3 h). For imaging, cells were transferred to the microscopy chamber of a confocal microscope (SP8, Leica, Wetzlar, Germany) with a controlled environment (37°C, 5% CO₂). Cells were unbiasedly selected based on fluorescence of transfectants, and images were acquired using a frame size of 512 \times 512 pixels in the green channel (488 nm excitation, 510–530 nm emission). Following an acquisition of pre-photo-uncaging images, photo-uncaging of caged-IP₃ was achieved by illumination (405 nm, 20% laser power) at a local region of interest (ROI, 3 \times 3 μ m) for a duration of 300 frames (400 ms/frame in Figure 5D, 136 ms/frame in Figure 5E) using the Fly mode. Fluorescence intensity in the ROI at each frame (F) was normalised by intensity at the beginning of photo-uncaging (F₀) and plotted against time. The area under the curve (AUC) was quantified for the duration of photo-uncaging to determine the amount of ER Ca²⁺ release.

Fluorescence lifetime imaging microscopy (FLIM)

Prior to FLIM experiments, SH-SY5Y cells (WT or KO lines) were transfected to express ER-Crowdedness or D4ER probe⁴¹ for luminal calcium measurements and RTN4a-SNAP for overexpression (see plasmid list for full details). Overexpression of RTN4a was monitored by labeling with SNAP-Cell 647-SiR. FLIM was carried out using a pulsed (80 MHz) wight light laser and HyDX or HyDS detectors in counting mode (STELLARIS8, Leica, Wetzlar, Germany). The excitation/emission was defined as 434/445–490



or 438/450–490 nm wavelength for D4ER and ER-crowding probes respectively. Images were acquired using a frame size of 512 \times 512 pixels, and settings were set to reach 5000 photons/pixel. Images were processed using Leica STELLARIS8 FLIM wizard. ROIs were drawn around individual cells and data fitted with a monoexponential decay function. [Ca²⁺ FLIM analyses performed as in our previous report. ⁴⁰ For D4ER, maximal calcium condition was determined as the ROI with minimal lifetime, and minimal calcium condition (corresponding to maximum lifetime) was obtained by adding thapsigargin (3 μ M, 5 h) into the culture media after baseline measurements.

Simulations of transport in ER tubular networks

Numerical simulations of intra-ER transport were carried out using a finite volume method (FVM), treating particle concentrations as continuous field variables defined on a network of one-dimensional edges connected at point-like junctions.

1. Network geometry. Two-dimensional cell-shaped domains were extracted from images of ER luminal marker in 8 COS-7 cells (same cells used for membrane protein spreading analysis in Figure 4C). The cytoplasmic domain was segmented as described in Methods for photoactivation analysis. The domain was filled with a regular honeycomb network structure of edge length 1 μ m, truncated at the domain boundaries.

Network edges were discretised into one-dimensional mesh cells of length δx , with $\delta x \leq 0.1 \ \mu m$. Each non-terminal junction node corresponded to a mesh cell of total length $\Sigma \delta xi/2$, where δxi is the mesh size on each of the adjacent edges.

2. Simulation of photoactivated particle spreading. The photoactivated center for each simulated cell was selected randomly, at a distance of 4–7 μ m from the nucleus. The photoactivated region consisted of all mesh cells centered within 1.4 μ m of the activation center.

The concentration of photoactivated particles (c) is assumed to evolve according to the advection-diffusion equation

$$\frac{\partial \mathbf{c}}{\partial t} = D \frac{\partial^2 \mathbf{c}}{\partial x^2} - v \frac{\partial \mathbf{c}}{\partial x}$$

with c = 1 fixed within the photoactivation region, and with reflecting boundaries at all terminals (degree 1) nodes in the network structure. Initial conditions were set to c = 0 outside the photoactivated region. Simulations with diffusion only have v = 0. Simulations including active flow set v = $\pm 20 \,\mu$ m/s, with the flow direction selected randomly along each network edge. The flow direction on each edge remains persistent over a timescale of τ = 0.1sec, with the flow reversal modeled as an independent Poisson process on each edge. At every time-step, for each edge, the flow direction is reversed with probability 1 – exp(-dt/ τ). The flow velocity magnitude was taken from prior measurements of luminal protein velocity distributions along ER network edges. ³¹ The persistence timescale τ was selected to be long enough for the flow to drive a protein along an average-length network edge. Modeling results on active networks indicate that such a persistence time leads to the most rapid spreading of particles across the network. ⁴⁸ The concentration field was evolved forward in discrete time-steps (dt = 5×10^{-5} sec), with forward Euler steps employed for the diffusive component (using a centered differencing method for the spatial differentiation) and a Lax-Wendroff scheme for the advective component. The choice of time step and mesh size satisfies the CFL criterion. Numerical convergence and stability were further established by testing that the resulting spatiotemporal concentration profiles were unchanged if either the mesh size or the timestep were decreased by a factor of two. Details of the finite volume numerical evolution scheme are provided together with our custom code (in Fortran 90; available on https://doi.org/10.5281/zenodo.11206293).

The resulting concentration profiles on the meshed network were processed into images comparable to those collected for experimental data. Namely, the concentration field at each time interval of 0.14 s was visualised (in MATLAB, with a grayscale colormap) and pixelated into a 512 \times 512 pixels image. The image was then blurred with a spatial Gaussian filter with σ = 1 μ m, and augmented with Gaussian noise with σ = 0.005 (concentration units). Resulting images were then processed to select wedge-shaped ROIs, trace ROI signals over time, and extract a characteristic half-time for the signal rise, exactly as for experimental data.

3. Simulation of calcium dynamics. Details of this model are provided in a prior article 37 ; an overview is included here for completeness. Our model for intra-ER calcium dynamics incorporates rapidly-equilibrated binding to calcium buffer proteins (with dissociation constant K_D), diffusion of free calcium ions (diffusivity D_c) and of buffer proteins (diffusivity D_p), and advective flow of velocity v. We consider the limit of fast calcium on and off rates, so that the calcium binding is assumed to be equilibrated at each time-step. The protein diffusivity is set to $Dp = 2.8 \ \mu m^2/s$, based on our latest single particle tracking measurements in the ER lumen. Prior measurements of cytoplasmic diffusivity of calcium and calcium-binding proteins indicate that free calcium diffuses on the order of ten times faster compared to bound calcium. We therefore set the diffusivity of free calcium in the ER lumen to be a factor of ten higher than the buffer proteins ($D_C = 28 \ \mu m^2/s$). The dissociation constant is taken as $K_D = 0.3 \ mM$, the initial free calcium concentration is set to be spatially uniform at 1 mM, and the initial concentration of buffer protein sites is set to 20 mM, in keeping with the weak binding strength and high calcium binding capacity of calreticulin proteins. 50

The evolution of two fields is tracked over time and space: U(x, t) represents the concentration of unbound calcium ions and S(x, t) represents the total concentration of buffer protein sites (including bound and unbound). The time evolution of these fields is defined by:

$$\frac{\partial (U+B)}{\partial t} = D_c \frac{\partial^2 U}{\partial x^2} + D_B \frac{\partial^2 B}{\partial x^2} - v \frac{\partial (U+B)}{\partial x}$$



$$\frac{\partial S}{\partial t} = D_B \frac{\partial^2 B}{\partial x^2} - v \frac{\partial S}{\partial x}$$

where B is the concentration of bound calcium ions, set at each time-step according to the equilibrium relation: $B = US/(U + K_D)$. The change in total protein (ΔS) and total calcium $\Delta (U + B)$ at each timestep is computed according to the usual finite volume approach (Euler forward step with centered spatial differences for the diffusive components, Lax-Wendroff scheme for the advective component). The corresponding change in free calcium is then given by:

$$\Delta U = \frac{\Delta (U + B) - \frac{U}{U + K_D} \Delta S}{1 + \frac{SK_D}{(U + K_D)^2}}$$

This approach explicitly maintains both equilibrium binding and mass conservation (in the absence of sources and sinks) over the time evolution.

This dynamic model is applied to an ER network extracted from a single confocal image of a COS-7 cells (one of the wildtype cells used for tubule width measurement in Figure 2C). The image analysis was done using publicly available machine learning-based llastik software for segmentation of a peripheral ER network structure, followed by the MATLAB "skeletonize" function and custombuilt code for grouping nearby nodes and tracing individual edges.

To model calcium release from the ER, we introduce a permeable region of radius 3 μ m and permeability coefficient p (units of length per time). For mesh cells within this region, a term of -2p/r \times U \times dt is added to the equation for Δ U above, where r is the tube radius.

The dynamic system is evolved forward with timesteps of 2×10^{-5} sec, for a total simulation time of 20 s. Random active velocities are represented as described for the photoactivated spread simulations, with 10 independent runs incorporating different realizations of the random velocity directions. Total calcium released from the permeable region is tracked over time by integrating the outward flux $2p/r \times U \times dt$ at each time-step. Thick lines in Figure 5A indicate the mean values over the 10 runs for each condition.

4. Rapid calcium release estimate. Our model for calcium dynamics relies on the assumption that the locally releasing region has a high effective permeability (p) for calcium to leak out of open ion channels, so that calcium release becomes limited by transport from elsewhere in the network. This assumption is justified by comparing to published measurements of calcium leakage rates and cytoplasmic elevations during localised release events. Specifically, measurements of calcium "blips" in *Xenopus* oocytes estimate the rate of release of calcium in a localised event at approximately 10^6 ions per second, released from a diffraction-limited region of the peripheral ER. Shathere is a 20-fold excess of Ca^{2+} binding sites in the lumen, whereas only the free calcium is allowed to leak out, we can estimate the overall rate for calcium leakage as $2p/r/(20) \times U \times \pi r^2 L$, where $L \approx 2 \,\mu m$ is an estimate of ER tubule length in the release region, $r \approx 0.05 \,\mu m$ is the tubule radius, and $U \approx 1 \,m M$ is the free calcium concentration. Matching to the reported leakage rate gives a permeability estimate of $p \approx 50 \,\mu m/s$.

Further, data on Ca^{2+} puffs in osteoclasts indicates that local cytoplasmic Ca^{2+} elevations on the order of \sim 1 μ M develop over a timescale of approximately 0.1 s. 53 The leaked Ca^{2+} from a localised event would spread diffusively in the cytoplasm over a volume that can be estimated as $V_{cyto} \approx 4/3 \ \pi \ (Dt)^{3/2}$, resulting in substantial dilution of the concentration in the cytoplasm over time. Assuming that a 'puff' event involves complete Ca^{2+} release from an L = 2 μ m stretch of ER tubule, and a cytoplasmic Ca^{2+} diffusivity of \sim 100 μ m²/s, the overall Ca^{2+} concentration in the cytoplasm would rise to 0.8 μ M, a concentration consistent with measurements. A permeability that is lower by an order of magnitude (p \approx 5 μ m/s) would allow only about 5% of the local Ca^{2+} in the release region to leak out during a 0.1 s interval, yielding cytoplasmic concentrations an order of magnitude lower than those observed. We therefore conclude that calcium release channels are sufficiently dense on the ER membrane so that local calcium resolves are depleted within subsecond time-scales, consistent with a high local permeability coefficient (p \approx 50 μ m/s). This high permeability assumption allows us to focus on the role of Ca^{2+} transport through the ER lumen as an important process limiting Ca^{2+} release rates. Similar estimates of the appropriate permeability for a local release region were obtained from a more detailed model of cytoplasmic Ca^{2+} elevation, as described in Crapart et al., 2024. It should be noted that the high permeability values estimated here can be achieved with relatively low surface densities (\sim 0.05% area coverage) of open channels on the ER membrane.

Neurite outgrowth analyses

The human iPSCs outgrowth assays were carried out using an automatic microscopy imaging system (Incucyte, Sartorius). Differentiation of parental iPSCs into iNeurons was induced as described above, and cells were seeded on day 3 on a 96-wells plate at a density of 20,000 cells per well. From day 4, cells were repeatedly phase-imaged every 3 h using a 20× objective. The resulting phase image stacks were analyzed using Incucyte neurite detection software (Sartorius), from which mask images of cell-body clusters and neurites were extracted. These images were then further processed through a custom Python code that 1. Computes the area covered by neurites and the number of different cell-body clusters and 2. Computes the neurite area and number of cell-body clusters for each well by adding the values obtained for the different field of view covering a well at each time point. The growth rates



from Figure 1D were obtained for each well by fitting a line to the normalised neurite area obtained by dividing the neurite area at each time point by the average area of cell-body clusters detected over all time points in this well.

Generation of RTN4 knockout cell lines by CRISPR

The 20-nucleotides (nt) sequence in the guide RNA (gRNA) targeting RTN4 (common region across all splicing variants) was designed using the CRISPR Design tool (https://www.atum.bio/eCommerce/cas9/input). Oligonucleotides encompassing the guide sequence and Bbsl (also known as Bpi1) restriction enzyme site overhangs (see the STAR Methods section) were annealed, phosphorylated by polynucleotide kinase (PNK), and sub-cloned into the vector that expressed Cas9 from Streptococcus pyogenes together with a GFP, pSpCas9-2A-GFP (Addgene #48138, Cambridge, MA, USA). 24 h post-transfection, single cells expressing gRNA and Cas9 were sorted by the cell sorter (FACS Melody, BD Biosciences, San Jose, CA) based on GFP fluorescence (SH-SY5Y and COS-7), or sorted manually (iPSCs). Each single clone was subjected to genomic DNA extraction and PCR to identify insertions and deletions (indels) by non-homologous end-joining (NHEJ). PCR products were subsequently sequenced using forward primers used in the PCR. Selected clones were subsequently subjected to immunoblot to confirm knockout at the protein level. Primer information is shown in the STAR Methods section.

Protein expression analyses

The cells were lysed by radioimmunoprecipitation assay (RIPA) buffer and protein concentrations of lysate were determined using a BCA Protein Assay Kit (#23225, Thermo Fisher Scientific Inc., Waltham, MA, USA). Equivalent amounts of proteins were subjected to sodium dodecyl sulfate-polyacrylamide gel electrophoresis (SDS-PAGE) and transferred to polyvinylidene fluoride (PVDF) membrane. The membranes were blocked and incubated with primary antibodies to RTN4 and β -tubulin at 1:1000 each. Fluorescent dye-conjugated secondary antibodies were used at 1:3000 and the proteins were detected using ChemiDoc MP Imaging System (Bio-Rad, Hercules, CA, USA).

QUANTIFICATION AND STATISTICAL ANALYSIS

Statistical analyses and visualisation were performed using Prism9. Error bars, *p* values, statistical tests and sample sizes are reported in the figure legends. All experiments were performed independently at least three times. Statistical differences between probability distributions were assessed using two-way Kolmogorov-Smirnov tests and statistical differences between distribution medians were assessed using two-sided Mann–Whitney U-tests.